Graduation Internship for the Master Technical Medicine
University of Twente

December 2023

In vivo validation of ultrafast ultrasound-based velocity vector imaging

Maxime J. P. Schoonbrood

In vivo validation of ultrafast ultrasound-based velocity vector imaging

Research report

Maxime J. P. Schoonbrood

Graduation Internship for the Master Technical Medicine
University of Twente

December 2023

Graduation committee

Chairman and technological supervisor

Prof. dr. ir. C. L. De Korte
Multi-Modality Medical Imaging Group, University of Twente
Medical Ultrasound Imaging Center, department of Medical Imaging, Radboudumc

Medical supervisor

Prof. dr. M. M. P. J. Reijnen
Department of Vascular Surgery, Rijnstate Hospital
Multi-Modality Medical Imaging Group, University of Twente

Technological supervisor

Dr. ir. A. E. C. M. Saris
Medical Ultrasound Imaging Center, department of Medical Imaging, Radboudumc

Process supervisor

E. M. Walter *MSc.*
Communication and professional behavior, Technical Medicine, University of Twente

Daily supervisor

J. M. K. de Bakker *MSc.*
Medical Ultrasound Imaging Center, department of Medical Imaging, Radboudumc

Daily supervisor

J. Ruisch *MSc.*
Department of Vascular Surgery, Rijnstate Hospital
Medical Ultrasound Imaging Center, department of Medical Imaging, Radboudumc

External member

Dr. ir. F. F. J. Simonis
Magnetic Detection and Imaging Group, University of Twente

Acknowledgements

About a year ago, I started my graduation internship for my master's degree in Technical Medicine at the University of Twente, Enschede, in collaboration with the Rijnstate hospital in Arnhem and the Radboud University Medical Center in Nijmegen. I got the opportunity to gain valuable experiences in clinical practice and used them to contribute to a technically challenging study. I have grown as a person and have developed myself professionally as a technical physician. None of this would have been possible without the support and guidance of a lot of people. I would like to thank a few of them in particular.

My deepest gratitude goes to my daily supervisors, Joosje and Janna. Joosje, I cannot thank you enough for the time and effort you put into helping me with all my (programming) questions. You were always there for me and made me feel part of the team. Janna, thank you for trusting me with a lot of responsibility. You taught me to make my own decisions, but were always willing to think along. I will not forget the interest both of you showed in me and the listening ear you offered when needed. I leave with a feeling of friendship and trust.

I would also like to express my appreciation to the rest of my graduation committee. Chris, you were mostly in the background, but offered me just the right encouragement at pivotal moments to steer me in the right direction. Michel, thank you for trusting me in making my own decisions while maintaining a genuine curiosity about my work. You made time to think along and your enthusiasm increased my motivation every time. Anne, you were always willing to engage in thoughtful discussions and asked inspiring questions that made me think. I admire the fact that you always thought about ending a meeting on a positive note with a small compliment which has brightened up my day many times. Elyse, you have guided me and supported me in getting to know myself. More than once you showed me a perspective I had not thought about myself. Frank, thank you for completing my graduation committee. During my studies, your lectures were my favorites. We shared a laughter many times and my love for MRI has grown because of you.

I would like to extend my gratitude to Joske, for her ability to teach me to see things in perspective during our intervision sessions. Suzan and Lonneke, I am very grateful that I got to know you both over the past year. We have supported one another along the way, but mostly took time to make a lot of fun. Thomas and Majorie, thank you for the collaboration and interesting exchange of ideas about my project.

Lastly, I would like to thank my parents and sister for their unconditional love and support throughout my studies. And my boyfriend, Jeroen, for standing with me along the way.

Abstract

Background A stroke is a serious life-threatening medical condition. Of all strokes, 10-15% follow thromboembolism after the rupture of an atherosclerotic plaque in the internal carotid artery. Yet, the current criteria for the selection of patients for carotid endarterectomy based on conventional ultrasound are highly inadequate and lead to both over- and undertreatment. With the advent of ultrafast ultrasound, a new velocity vector imaging technique based on blood speckle tracking has been developed at the Radboud University Medical Center in Nijmegen, for the visualization of complex blood flow patterns that are associated with onset, progression, and rupture of atherosclerotic plaques. The visualization and quantification of complex blood flow patterns may enable better patient-specific risk assessment.

Objective The aim of this research is to evaluate the performance of ultrafast ultrasound-based velocity vector imaging using blood speckle tracking in the carotid artery of healthy volunteers in comparison to 4D flow MRI.

Methods This validation study included 20 healthy volunteers that underwent both ultrafast ultrasound-based velocity vector imaging and 4D flow MRI of the carotid artery. A semi-automatic algorithm was designed to perform registration of MRI to ultrasound based on segmentations of the carotid artery. The similarity of the registered planes was calculated based on the structural similarity index metric. Both techniques were compared qualitatively using temporal and spatial velocity profiles and quantitatively with a cosine similarity index of the velocity vector fields and a root-mean-square error of the correlation for axial and lateral velocity magnitudes.

Results The semi-automatic registration algorithm resulted in a registration for 7 volunteers, with a median structural similarity index of 0.94 [0.71 – 0.97]. The temporal and spatial velocity profiles showed fairly good correspondence. The median [min – max] cosine similarity for reliable velocity vector estimates was 0.77 [0.68 – 0.87] and the percentual RMSE for axial and lateral velocity magnitudes were 36% and 22%, respectively.

Discussion The registration of MRI to ultrasound is uncertain due to the low resolution of the MRI scan, which affects the reliability of the outcomes. Also, the lower temporal and spatial resolution of 4D flow MRI relative to ultrasound velocity vector imaging hinder the validation of short-lived events that underlie complex blood flow. Nevertheless, this study is a first step towards the in vivo validation of ultrafast ultrasound-based velocity vector imaging and underwrites its potential for implementation in future clinical practice.

Keywords Atherosclerosis, Blood velocity estimation, Carotid artery, Ultrasound velocity vector imaging, 4D flow MRI.

List of Abbreviations

CEA	Carotid endarterectomy
ECA	External carotid artery
ECG	Electrocardiography
ICA	Internal carotid artery
MR	Magnetic Resonance
MRI	Magnetic Resonance Imaging
PRF	Pulse repetition frequency
PSV	Peak systolic velocity
RF	Radiofrequency
RMSE	Root-mean-square error
ROI	Region of interest
SSIM	Structural similarity
TIA	Transient ischemic attack
VENC	Velocity encoding
WSS	Wall shear stress

Table of Contents

1. Introduction 1
2. Research question and hypothesis 3
3. Technological background 3
   3.1 Ultrafast ultrasound-based velocity vector imaging 3
      3.1.1 Ultrafast ultrasound 3
      3.1.2 Clutter filtering 4
      3.1.3 Velocity vector estimation methods 4
      3.1.4 Blood speckle tracking 5
      3.1.5 Adaptive velocity compounding 5
   3.2 4D flow Magnetic Resonance Imaging 6
4. Methods 8
   4.1 Study design and population 8
   4.2 Data acquisition and post-processing 8
      4.2.1 Ultrasound-based velocity vector imaging 8
      4.2.2 4D flow MRI 10
   4.3 Registration algorithm 11
      4.3.1 Pre-processing 11
      4.3.2 Search for the matching slice 12
      4.3.3 Outcome measure 14
   4.4 Comparison of the velocity vectors 14
      4.4.1 Pre-processing 14
      4.4.2 Evaluation and outcome measures 15
5. Results 15
   5.1 Cohort characteristics 15
   5.2 Outcomes of the registration algorithm 16
   5.3 Outcomes of the comparison of the velocity vectors 18
6. Discussion 23
   6.1 Interpretation of the results 23
   6.2 Limitations of the study 24
   6.3 Recommendations for future research 25
7. Conclusion 26

1. Introduction

Every three seconds, someone around the world suffers a stroke. [1] A stroke is a serious life-threatening medical condition that is characterized by damage to the brain and eventual cell loss due to a lack of oxygen supply. It is the second-leading cause of death and third-leading cause of disability worldwide. [2] There are two types of strokes: hemorrhagic and ischemic strokes. Hemorrhagic strokes are less common, but often more severe, and result from a bleeding following the rupture of an artery in the brain. Ischemic strokes account for the vast majority of strokes and are caused by the disruption of blood flow to part of the brain. If the disruption of blood flow is temporary, with full recovery of symptoms within 24 hours, we speak of a transient ischemic attack (TIA). The disruption of blood flow to the brain is either due to the narrowing or occlusion of a cerebral artery by buildup of atherosclerotic plaque in the vessel wall or caused by blockage by an embolus. Of all strokes, 10-15% follow thromboembolism after the rupture of an atherosclerotic plaque in the internal carotid artery. [3] Therefore, the condition of the vasculature supplying blood to the brain is investigated in patients who suffered an ischemic stroke or TIA.

Duplex ultrasonography is the first-line diagnostic imaging modality to assess the presence and degree of carotid artery stenosis. Duplex ultrasonography includes the evaluation of atherosclerotic plaque morphology on B-mode imaging and Doppler velocity measurements of the common carotid artery, internal carotid artery (ICA), and external carotid artery (ECA). The outcomes may be verified by contrast enhanced Computed Tomography or Magnetic Resonance (MR) angiography. Patients with a carotid artery stenosis are prescribed medical treatment, including antihypertensive drugs, anti-thrombotic agents, and cholesterol synthesis inhibitors to prevent recurrent strokes and other cardiovascular events. [4] In addition, patients may be eligible for an intervention. Carotid endarterectomy (CEA), surgical removal of the plaque, is considered the gold standard. CEA is recommended for symptomatic patients with severe ICA stenosis (≥70%), which is diagnosed sonographically when ICA peak systolic velocity (PSV) is ≥230 cm/sec together with a visible luminal narrowing (≥50%). In symptomatic patients with moderate ICA stenosis (50-70%), i.e. ICA PSV between 125 and 230 cm/sec together with a visible luminal narrowing (≥50%), CEA can be considered based on the carotid artery risk score. [4], [5] This score predicts the five-year risk of ipsilateral stroke with medical treatment alone. [6] In case of asymptomatic patients, CEA is only considered for men under 75 years of age with a severe ICA stenosis if the surgical risk of a disabling cerebral infarction, cerebral hemorrhage or death is below 3%. Carotid artery stenting is an alternative to CEA in a selected group of patients. [4] However, the aforementioned criteria for the selection of patients for intervention are highly inadequate. The *number needed to treat* is six for patients with severe ICA stenosis. [7] This means that with every six interventions only one recurrent stroke is prevented within five years, while five patients are unnecessarily exposed to the risks of surgery. Moreover, patients with symptomatic mild ICA stenosis (20-49%), who only receive medical treatment, have a 7.4% chance of suffering a recurrent stroke within three years, which might have been prevented with early intervention. [8] The both over- and undertreatment show the need for improved patient-specific risk stratification for a better selection of patients who will benefit from intervention.

Patient-specific risk stratification requires understanding of the mechanisms underlying onset, progression, and rupture of atherosclerotic plaques. One of the mechanisms that plays an important role in all stages of atherosclerotic cardiovascular disease is wall shear stress (WSS). WSS is the tangential stress exerted by the flowing blood on the endothelial surface of the arterial wall. Normal maximum WSS in arteries is considered to be between 1 and 7 Pa. [9] Low and/or

oscillating WSS can be associated with onset and progression of atherosclerosis. In contrast, high WSS values at the site of the stenosis make the atherosclerotic plaque more prone to rupture. A rupture causes the highly thrombogenic core of the plaque to be exposed to the blood, thereby increasing the risk of the formation of a blood clot that can break loose and lead to an ischemic stroke or TIA. Abnormally low and high WSS values occur mainly at locations of geometrical irregularities, like the carotid bifurcation, as a result of locally disturbed and complex blood flow patterns. [10], [11] Therefore, visualization and quantification of complex blood flow patterns may enable the estimation of WSS and other flow-derived parameters, that can be used for better patient-specific risk assessment of recurrent stroke.

Conventional color Doppler ultrasound visualizes solely the axial component of blood flow velocity, i.e. in the direction of the ultrasound beam. The true blood velocity can be derived only in a single sample volume using pulsed wave Doppler with manual angle correction, which makes the technique susceptible to operator-dependent errors. Besides, the detection of short-lived events is limited by the low frame rate due to the line-by-line acquisition method. Complex blood flow can variate strongly in direction and magnitude over space and time. [12] Consequently, conventional Doppler ultrasound methods are unable to visualize complex blood flow patterns. However, with the advent of ultrafast ultrasound, new possibilities have arisen for the development of techniques to visualize complex blood flow patterns using 2D velocity vectors at any location in the image plane. [13]–[15] These techniques are commonly referred to as velocity vector imaging.

At the Medical Ultrasound Imaging Center of the Radboud University Medical Center in Nijmegen, the Netherlands, Saris *et al.* [16] developed an ultrafast ultrasound-based 2D velocity vector imaging method using blood speckle tracking in the carotid artery. The method has proven to be able to visualize and quantify complex flow patterns with high accuracy and precision in an experimental setup. Moreover, the first in vivo recordings were promising for the clinical feasibility of the method. The introduction of the method in clinical research could increase our understanding of complex flow patterns in relation to onset, progression, and rupture of atherosclerotic plaques, for patient-specific risk stratification. Therefore, in vivo validation of the 2D velocity vector imaging method is necessary to gain insight in the accuracy and reproducibility in human subjects.

Currently, 4D (3D + time) flow MRI is the only non-invasive blood flow velocity quantification technique that is clinically validated for flow measurements and it is therefore considered the in vivo gold standard. [17] 4D flow MRI uses velocity-encoding to measure the velocity magnitude in three perpendicular directions based on phase-contrast, allowing for the calculation of a 3D velocity vector at any location in the image volume. [18] Yet, MRI has some important disadvantages relative to ultrasound. It is much more expensive and less easily accessible, has a higher burden for the patient, no live view, and a lower temporal and spatial resolution. Therefore, ultrasound remains the technique of choice for the screening of the carotid artery. The aim of this research is to evaluate the performance of ultrafast ultrasound-based velocity vector imaging using blood speckle tracking in the carotid artery of healthy volunteers in comparison to 4D flow MRI.

2. Research question and hypothesis

The research question that is being answered in this thesis is:

> How does the performance of ultrafast ultrasound-based velocity vector imaging using blood speckle tracking compare to 4D flow MRI in assessing the velocity vector field in the carotid artery of healthy volunteers?

Two sub questions underlying the research question are:

1. How can the 4D flow MRI volume be registered to the ultrafast ultrasound-based velocity vector imaging plane?
2. How can velocity vectors obtained from ultrafast ultrasound-based velocity vector imaging be compared with those from 4D flow MRI?

Previous research by Saris *et al.* [16] confirmed the reliability of the ultrafast ultrasound-based velocity vector estimates based on a high level of correspondence with conventional ultrasound imaging in straight-tube measurements and in vivo in two healthy and three diseased carotid arteries. Therefore, it is hypothesized that the performance of ultrafast ultrasound-based velocity vector imaging using blood speckle tracking will demonstrate comparable to 4D flow MRI in assessing the velocity vector field in the carotid artery of healthy volunteers. However, it is expected that 3D-to-2D registration of two different imaging modalities is complicated and may influence the results. Furthermore, it is anticipated that the enhanced temporal and spatial resolution of velocity vector imaging will provide more detailed insights into complex blood flow patterns in the carotid artery that may go undetected by 4D flow MRI.

3. Technological background

In this study, two imaging techniques for the visualization of blood flow velocity patterns in the carotid artery are compared. This chapter describes the technological background and working principles of both techniques.

3.1 Ultrafast ultrasound-based velocity vector imaging

Velocity vector imaging is a collective term for relatively new techniques that allow for angle-independent estimation and visualization of blood velocity patterns. Velocity estimation is performed not only along the axial direction, as is the case for conventional color Doppler ultrasound, but also along another direction of the image plane. This allows for the evaluation of the magnitude and direction of the velocity vector at any location in the image plane.

3.1.1 Ultrafast ultrasound

Ultrasound imaging is based on the transmission of high frequency sound waves into the body and receiving their reflections and scattering of body structures. In conventional line-by-line ultrasound imaging, a focused ultrasound pulse is transmitted into the tissue and the received echoes are used to reconstruct a single line of the image. The frame rate (of around 10-30 frames/sec) is limited by the number of image lines multiplied with the time required to transmit a pulse and receive the backscattered echoes. With the advent of ultrafast ultrasound, it is possible to obtain ultrasound images with a much higher frame rate (up to 10000 frames/sec). Ultrafast ultrasound imaging uses the transmission of an unfocused plane wave that insonifies the full field-of-view at once. [15] Reconstruction of all image lines takes place simultaneously, using parallel receive beamforming (e.g. delay-and-sum beamforming). [19] Higher frame rates allow for higher temporal resolution. Moreover, the short time between subsequent frames opened up possibilities for new velocity vector

estimation methods, like blood speckle tracking, that otherwise would suffer from decorrelation of the speckles between image frames. A limitation of ultrafast ultrasound is that it suffers from low lateral spatial resolution and low contrast, since focusing is restricted to the receive mode. The image quality can be improved, partially at the cost of the frame rate, by combining multiple tilted plane waves to obtain one image plane using coherent compounding. [20]

3.1.2 Clutter filtering

The signal that is measured for the visualization of blood flow originates from the scattering of red blood cells. The amplitude of the backscattered echoes from red blood cells is typically far less than the amplitude of the reflections from surrounding structures. The removal or suppression of clutter signal, originating from surrounding tissues, is therefore a major challenge in blood velocity vector imaging. [21] Conventional clutter filtering is based on the difference in temporal frequency between the relatively fast moving blood and the slow moving of nearly stationary surrounding tissue. The signal from the surrounding tissue can be suppressed by applying a high-pass filter in the frequency domain, see Figure 1. There is a trade-off between sufficient stopband attenuation, to remove the clutter signal, and the steepness of the transition region, to minimize the loss of blood signal. [22] In the velocity vector imaging technique developed by Saris *et al.* [16], adaptive high-pass finite impulse response clutter filtering is applied over the cardiac cycle. It uses a short transition region with a dynamic cut-off value that is set based on the axial vessel wall velocities. Several other clutter filter designs have been suggested [23], but they will not be mentioned here.

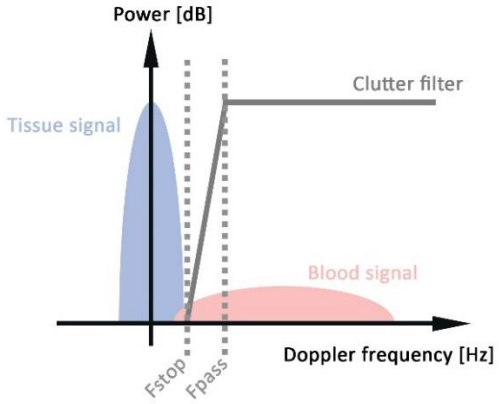

Figure 1 High-pass clutter filtering. [22]

3.1.3 Velocity vector estimation methods

The estimation of the velocity vectors can be based on four types of estimation principles: multi-angle Doppler analysis, transverse oscillation, directional beamforming, and speckle tracking. [13] Multi-angle Doppler analysis uses triangulation to combine 1D Doppler estimates from different angles of insonation to derive a 2D velocity vector. [24] Transverse oscillation estimates the 2D velocity vector by introducing lateral oscillations in the ultrasound field by applying an apodization function in receive or by filtering around a desired lateral oscillation frequency in the Fourier domain. In this way, the received signals become sensitive to axial and lateral motion within the field. [25] Both multi-angle Doppler and transverse oscillation are based on the estimation of the phase-shift and are therefore limited by aliasing. In directional beamforming, the cross-correlation of beamformed lines between

subsequent acquisitions is calculated for multiple angled beamforming grids. The angle with the highest correlation value is used to calculate the magnitude and direction of the 2D velocity vector. This method has an intensive computational burden. [26] Lastly, blood speckle tracking uses the displacement of the blood speckle pattern between subsequent acquisitions to determine the 2D velocity vector. The blood speckle tracking technique is discussed more extensively hereafter, since it underlies the velocity vector imaging technique developed by Saris *et al.* [16] that is investigated in this study.

3.1.4 Blood speckle tracking

Blood speckle tracking is based on the principle that transmitted ultrasound waves are scattered in all directions when they encounter structures with dimensions smaller than the wavelength of the ultrasound, like red blood cells. The backscattered echoes form an interference pattern, called a speckle pattern. These patterns are tracked between subsequent acquisitions to determine the displacement of the tissue (i.e. blood), see Figure 2. A kernel region in one acquisition is matched to a larger search region in the subsequent acquisition, using a pattern matching function. The displacement of the underlying tissue is defined by the location that best matches the kernel region relative to the original location of this kernel. The velocity can be calculated by dividing the estimated displacement by the time between the frames used for displacement estimation. Saris *et al.* [16] use 2D normalized cross-correlation as pattern matching function. The procedure is repeated for the entire region of interest (ROI), which is manually outlined, to create a map of 2D blood velocity vectors. [22]

The performance of the blood speckle tracking method depends on the type of signal (radiofrequency (RF) or envelope) that is used and the sizes of the kernel and search region, which determine the robustness, computational time, and maximum detectable velocity. An important disadvantage of blood speckle tracking is its susceptibility to decorrelation of speckle patterns. This decorrelation can be a consequence of out-of-plane movement, strong velocity gradients, and low beam-to-flow angles. [22]

3.1.5 Adaptive velocity compounding

Saris *et al.* [16] proposed an adaptive velocity compounding method to further improve the accuracy of the blood velocity estimates. First, this method automatically adjusts the effective pulse repetition frequency (PRF) over the cardiac cycle. This allows for more accurate estimation of both low velocities in diastole and high velocities in systole with a low and high PRF, respectively. Secondly, a combination of displacement compounding [27] and compound speckle tracking [28] is applied. In this combined technique, two plane waves are transmitted into the medium at angles of -20° and 20°. The velocities are estimated for both angles separately. Then, the quality of the velocity estimates is determined. Saris *et al.* [16] perform this quality assessment based on the signal power after clutter filtering and the variance of the axial inter-frame velocities over 40 estimates. The 2D cross-correlation coefficient is used as a quality metric. When the velocity estimates of both angles are of sufficient quality, triangularization of the axial angular displacement component of both angles is performed. The axial component has the highest accuracy, because of the higher axial resolution and the presence of phase information in the axial direction of the RF data. If the velocity estimates of one of the angles is of too low quality, projection of the remaining angular velocity vector with sufficient quality is used to obtain the axial and lateral displacement component. In this way, the combined technique has the possibility to discard unreliable velocity estimates.

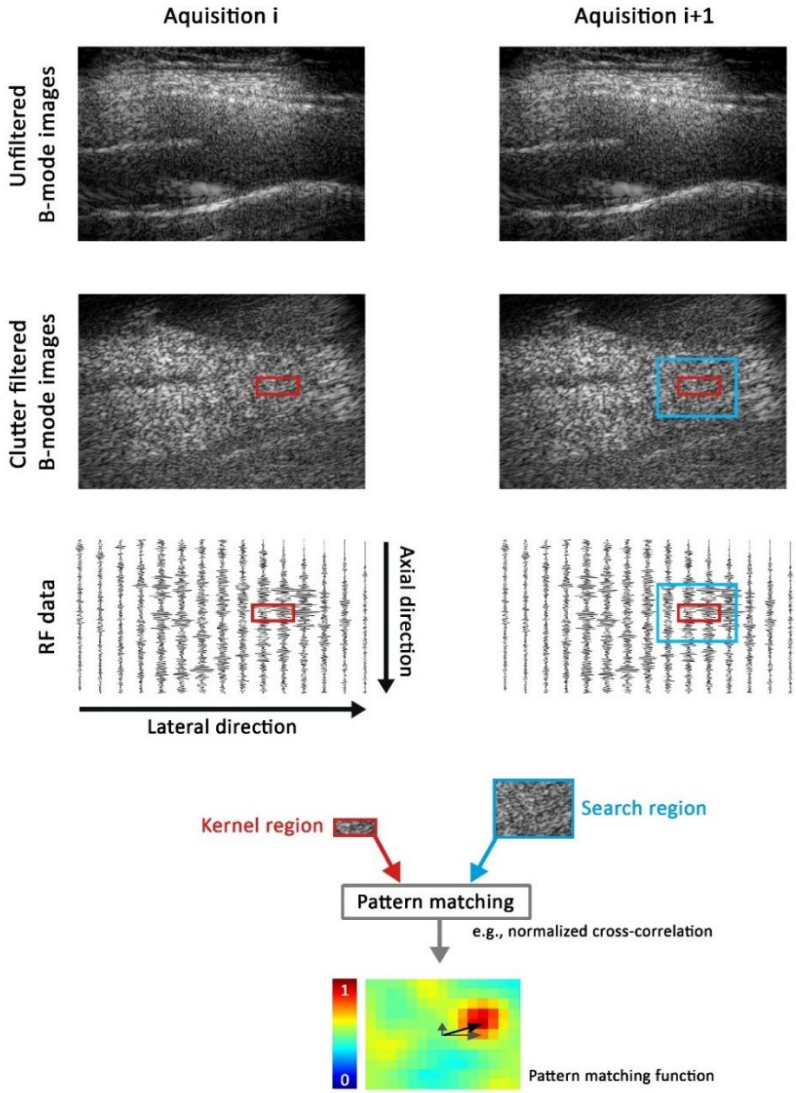

Figure 2 The basics of speckle tracking. Unfiltered B-mode images show the carotid artery bifurcation (top row), where the blood signal becomes visible after clutter filtering (second row). A kernel region in the first acquisition (i) is matched to part of a larger search region in the following acquisition (i+1). Matching is based on the underlying RF or envelope data (third row). The peak in the pattern matching function reveals the displacement (bottom row). [22]

3.2 4D flow Magnetic Resonance Imaging

Time-resolved three-dimensional phase-contrast MRI, known as 4D (3D + time) flow MRI, is based on the linear relationship between blood flow velocity and the phase of the MRI signal that is acquired during an MRI measurement. The MRI signal originates from hydrogen protons which constitute a large portion of body tissue and especially blood plasm, in contrast to the ultrasound signal which results from the scattering of red blood cells. [29] Flow MRI uses bipolar gradients to induce velocity-encoding in the x, y, and z direction. The effect of a bipolar gradient in one direction on stationary and moving hydrogen protons is illustrated in Figure 3. When the first half of the bipolar gradient is applied, protons undergo a phase shift depending on their location along the gradient. Protons that are moving, experience differing gradient strengths as their locations along the gradient are constantly changing. Therefore, they will have a different phase shift than

the surrounding stationary protons. When the second half of the bipolar gradient is applied with equal but negative magnitude, the phase shift of the stationary protons is nullified. However, the moving protons are all encoded with a phase shift. This phase shift is proportional to their velocity in the direction of the gradient. Faster moving protons will have a greater phase shift than slower moving protons, since they have experienced a greater difference in gradients. This process can be repeated for the x, y, and z direction to determine the phase shift and corresponding velocity component of flow in each direction. The velocity vector of a specific voxel encompasses all three measured velocity components. [30], [31]

Equation 1 shows the proportionality of the phase shift to the proton velocity and the gradient strength.

$$\Delta\varphi = \gamma\vec{v}\Delta M_1 \qquad [1]$$

With $\Delta\varphi$ the phase shift, γ the gyromagnetic ratio, $\vec{v}$ the proton velocity, and ΔM_1 the change in magnetic moment that is directly proportional to the gradient strength.

There is a maximum proton velocity that can be measured, since phase shifts that exceed 180° in the positive or negative direction will result in aliasing. This maximum velocity is set as a parameter, called the velocity encoding (VENC). This VENC is inversely proportional to the strength of the velocity-encoding gradients. It can be increased by decreasing the gradient strength and vice-versa. The spatial resolution for small velocities decreases with increasing VENC. In practice, it is therefore important to select the most appropriate VENC for the velocities to be measured. [31]

MR acquisitions are too slow to capture the dynamics within a single cardiac cycle in real time with sufficient spatial resolution. Consequently, the acquisition is split over multiple heartbeats. The acquisitions of multiple cardiac cycles are synchronized with the RR-interval by ECG-gating. The velocity vector fields are an average of acquisitions at specified phases during the cardiac cycle over multiple heartbeats. An advantage of 4D flow MRI is that it allows for retrospective positioning of analysis planes at any location withing the acquisition volume. This feature will be used in this study after the registration of the MRI volume to the ultrasound plane. [18]

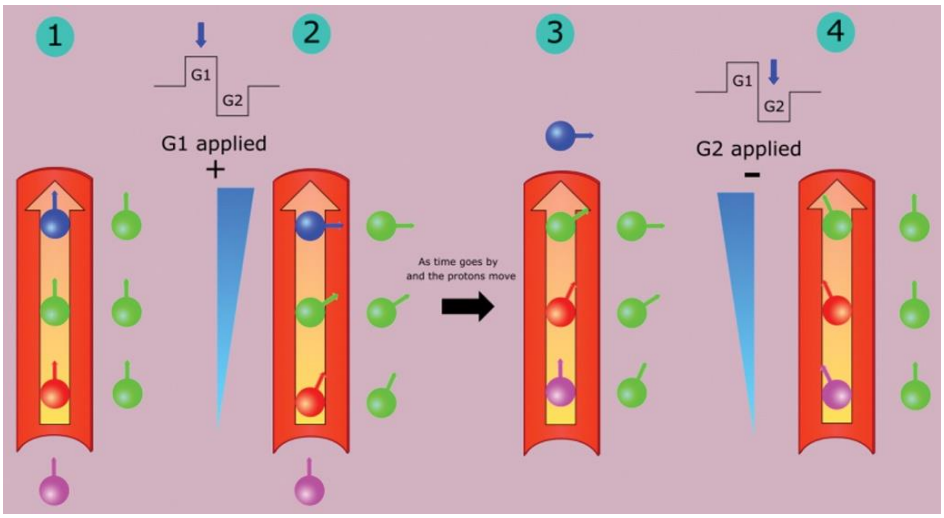

Figure 3 Application of a bipolar gradient in the direction of flow results in a phase shift in the moving protons. [31]

4. Methods

The method section describes the study design and population, data acquisition and post-processing steps for both ultrasound and MRI, the registration algorithm, and comparison methods for the velocity vectors.

4.1 Study design and population

This prospective, observational, validation study included 20 healthy volunteers, equally divided in two age groups of 20 to 30 and 65 to 75 years old with an equal distribution of men and women. The exclusion criteria were a cardiovascular or pulmonary medical history, the use of medication for cardiovascular risk factors, and standard MRI exclusion criteria (such as claustrophobia, the presence of a pacemaker or cerebral vascular clips). Volunteers who met the criteria were included in the study after they provided informed consent. Both ultrasound and MRI measurements were acquired of all participants and performed between November 2022 and March 2023 at the Rijnstate Hospital, Arnhem, the Netherlands. The study protocol conforms to the ethical guidelines of the 1975 Declaration of Helsinki and was priorly approved by an authorized ethical committee in the Netherlands (NL80478.091.22). Funding was obtained from the *Rijnstate Vriendenfonds*.

4.2 Data acquisition and post-processing

4.2.1 Ultrasound-based velocity vector imaging

Ultrafast ultrasound data was acquired using a programmable Vantage 256 ultrasound system (Verasonics, Kirkland, Washington, USA) equipped with an L12-5 50 mm linear array transducer (ATL, Bothell, Washington, USA) with a center frequency of 7.8 MHz. Plane waves were repeatedly transmitted at angles of -20° and 20° with a PRF of 10 kHz and data was acquired for 3 seconds, together with 3-lead ECG-recording. The active aperture (128 of 256 elements) for the -20° and 20° steered plane waves was chosen to obtain maximum overlap at the center of the carotid artery. An overview of the transducer properties and acquisition parameters is given in Table 1. The measurements were performed by a technical physician (JR) with 2 years of experience and participants were examined in supine position with their heads tilted slightly upward and to the right. The left carotid artery bifurcation was visualized in a longitudinal view. Whenever anatomically possible, the ICA and ECA were captured in one image view. Otherwise, the image plane was focused on the carotid bulb and the ICA.

Table 1 Ultrasound transducer properties and acquisition parameters

Property	Value
Center frequency (MHz)	7.8
Sampling frequency (MHz)	31.2
Transducer element pitch (μm)	195.3
Number of transducer elements	256
Number of simultaneously active elements	128
Elevational focus depth (mm)	18
Pulse repetition frequency (kHz)	10
Transmit and receive angle (°)	±20
Apodization window in transmit	Tukey (150, 30%)

Multiple post-processing steps were executed to obtain velocity vector estimates from the ultrafast ultrasound data. First, the RF channel data was beamformed using delay-and-sum beamforming on a point-spread-function-shaped beamforming grid. For velocity compounding, beamforming took place at angulated grids in the direction of the steered plane waves. For visualization of the data as B-mode images, the RF data of both angles was beamformed on a 0° grid and coherently compounded. A manually drawn vessel wall contour was tracked over all acquired frames to generate lumen ROIs and obtain the axial velocity component of the vessel wall. The data was clutter filtered using a 150th order Finite Impulse Response clutter filter with a -48 dB cut-off velocity of two times the 90th percentile axial vessel wall velocity and a short transition region of 1 cm/s (-80 till 0 dB). The clutter filter settings were dynamically set for angles of -20° and 20° separately. In order to suppress enough tissue signal during the diastolic phase, the minimum cut-off velocity was set to 0.1 cm/s. The blood velocity vectors were coarsely estimated using the cross-correlation of envelope data and thereafter the estimates were refined using RF data. Displacement estimation took place at an effective PRF of either 2.5 or 5 kHz, which was set per ensemble of 40 frames. If the 95th percentile of the estimated velocity magnitude in the first inter frame displacement estimate of the ensemble was below 0.25 m/s (estimated at an effective PRF of 5 kHz), displacement estimation took place at 2.5 kHz for the entire ensemble of 40 frames, otherwise a PRF of 5 kHz was used. The choice for performing compounding of both axial estimates or projection of a single angle axial and lateral estimate was based on the maximum cross-correlation coefficient. The threshold for reliable estimates was set at a correlation value higher than 0.4 for 15 out of the 40 ensemble estimates for each angle separately. In case both angles fulfilled this criterion, compounding was applied to all axial interframe displacement estimates of this spatial position. In case only one of the angles met the criterion, the axial and lateral displacement estimates of that one angle were projected. When none of the angles reached the criterion, compounding of the axial estimates was used to obtain a velocity vector, but the vector was marked as unreliable. Eventually, the median of the interframe displacements of each ensemble of 40 frames was calculated after spatial filtering to obtain the final ensemble velocity vectors. The post-processing settings for ultrafast ultrasound are summarized in Table 2.

Table 2 Ultrasound post-processing settings for beamforming and displacement estimation

Property	**Value**
Beamforming	
F-number	0.875
Apodization window in receive	Hamming
Sampling beamforming grid (µm), axial x lateral	12.3 x 51.7
Displacement estimation	
Template size (mm), axial x lateral Iteration 1 Iteration 2	 2.33 x 2.33 1.2 x 1.2
Median filtering interframe estimates (mm), axial / lateral Iteration 1	 0.5 x 0.5 / 0.5 x 0.5
Median filtering ensemble averaged estimates (mm), axial / lateral	0.25 x 0.25 / 0.25 x 0.25
Final displacement resolution (mm), vertical x horizontal	0.1 x 0.1

4.2.2 4D flow MRI

In addition to the ultrafast ultrasound imaging, all participants underwent a time-resolved phase-contrast 3.0T MRI scan (Ingenia, Philips Healthcare, Best, the Netherlands) with the use of a head-and-neck coil. Median [min – max] time between ultrasound and MRI measurements was 2 [0 – 133] days. The carotid artery bifurcation was localized in multi-section 2D survey acquisitions and a 3D quantitative flow scout scan was used to extract the PSV from the central area of a cross-section of the common carotid artery. The VENC was set at a value approximately 10% above the maximum PSV measured with MRI or conventional pulsed wave Doppler ultrasound, to prevent aliasing. Subsequently, a 3D acquisition was performed with a free-breathing RF-spoiled gradient echo sequence with 3-directional velocity encoding. Retrospective ECG-gating was used to reconstruct the cardiac cycle into 28 phases. The repetition time and echo time varied between participants due to a difference in heart rate, but there median [min – max] values were 4.549 [4.287 – 4.938] ms and 2.671 [2.418 – 3.012] ms, respectively. The flip angle was 8°. Images were acquired in a coronal plane with a resolution of 1.2093 x 1.2093 mm, 1.21 mm spacing between slices, and a slice thickness of 2.293 mm. The median [min – max] acquisition time was 11.7 [9.1 – 18.4] minutes. The MRI acquisition parameters are assembled in Table 3. Scans were executed by an MRI radiographer together with a technical physician with the participants again in supine position and their heads tilted slightly upward and to the right, to resemble their position during the ultrasound measurements.

Table 3 4D flow MRI acquisition parameters for all twenty volunteers

Property	Value
Spatial resolution (mm^3)	1.2093 x 1.2093 x 1.21
Slice thickness (mm)	2.293
Flip angle (°)	8
VENC (cm/s), median [min – max]	100 [75 – 150]
TR (ms), median [min – max]	4.549 [4.287 – 4.938]
TE (ms), median [min – max]	2.671 [2.418 – 3.012]
Total acquisition time (minutes), median [min – max]	11.7 [9.1 – 18.4]

Post-processing of the data, including offset correction for static tissue and anti-aliasing correction, was performed using CAAS MR Solutions software (Pie Medical Imaging, Maastricht, the Netherlands). This resulted in four datasets per volunteer for the MRI recordings: one 3D volume with magnitude information and three 3D volumes with phase information in the x, y, and z direction. The phase information in each direction was converted to velocity magnitudes, using Equation 2.

$$Velocity = rescale\ slope \cdot phase + rescale\ intercept \qquad [2]$$

The direction of positive flow is along the x-axis, from right-to-left, along the negative y-axis, from feet-to-head, and along the z-axis, from anterior-to-posterior, as shown in Figure 4.

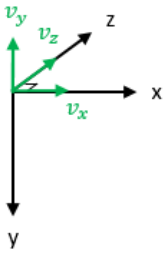

Figure 4 Direction of positive flow relative to the coordinate system x, y, and z-axis.

4.3 Registration algorithm

To be able to compare the velocity vectors of ultrasound-based velocity vector imaging to 4D flow MRI, it is necessary to extract the slice from the 3D MRI volume that corresponds with the 2D ultrasound plane. In other words, the 3D MRI scan should be registered to the 2D ultrasound plane. 3D-to-2D registration is a complex and difficult process, especially for images from different imaging modalities based on different physical properties. In this study, a semi-automatic algorithm was designed and evaluated to search for the slice through the 3D MRI scan that best matches the ultrasound plane based on geometrical information, namely the segmentations of the carotid artery on both scans. The algorithm is developed using MATLAB (R2021a, MathWorks, Natick, Massachusetts, USA).

4.3.1 Pre-processing

It was decided to match the MRI volume and ultrasound plane at the timepoint of PSV. The timepoint of PSV can be determined from the ultrafast ultrasound-based velocity trace at a manually appointed location in the ROI for one RR-interval of the cardiac cycle. It was assumed that the time between R-top on ECG to timepoint of PSV on the ultrasound velocity trace did not significantly change with varying heart rate. [32], [33] Therefore, the time t from R-top on the ECG to timepoint of PSV of the ultrasound velocity trace was divided by the duration d of one phase on MRI at the specified heart rate, to obtain the expected phase of PSV of the MRI scan, according to Figure 5.

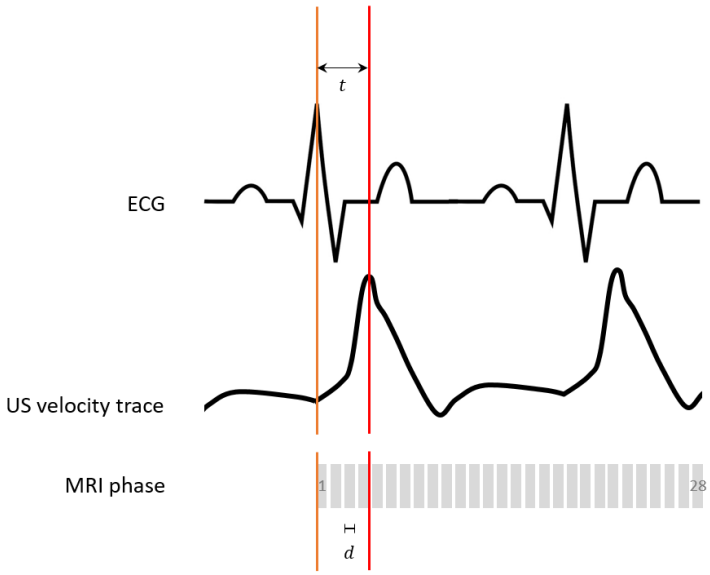

Figure 5 Time t from R-top on ECG to timepoint of PSV of the ultrasound velocity trace divided by the duration d of one phase on MRI at the specified heart rate, to obtain the expected phase of PSV of the MRI scan.

The carotid artery was segmented manually on the ultrasound frame at PSV. Unlike the post-processing steps of the ultrasound data, the entire image plane was used for this segmentation and not just the part where the steered plane waves overlap. This resulted in a binary 2D image with ones inside the lumen ROI and zeros outside the lumen. For registration purposes, the resolution of this binary image was reduced to match the resolution of the MRI scan. This was achieved through spatial averaging, resulting in an image of 29 x 21 pixels.

The MRI volume containing the magnitude information at PSV was cropped around a manually selected center point in the carotid artery bifurcation to limit the dimensions of the search volume to 71 x 51 x 31 pixels. The triangle method [34] was then used to calculate a threshold for segmentation of the lumen area based on a histogram of the normalized data of the cropped magnitude scan. The triangle method constructs a line between the peak of the histogram and the farthest bin that contains any pixels, as illustrated in Figure 6. The threshold is set at the value where the perpendicular distance from this line to the histogram is maximized. The automatic segmentations were visually evaluated and if necessary erosion and dilation with a structuring element or manual adjustments were executed. In this way, the final binary 3D search volume was obtained.

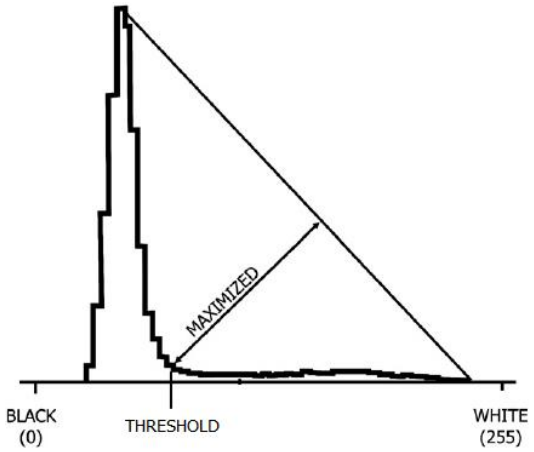

Figure 6 Triangle method to automatically determine the threshold for segmentation of the cropped MRI scan, adapted from [34].

4.3.2 Search for the matching slice

The search algorithm is designed to compare slices in multiple directions through the 3D binary MRI volume with the 2D binary ultrasound plane. Therefore, the cropped MRI volume is translated in the x, y, and z direction over varying distances and rotated around the x, y, and z-axis with multiple combinations of angles. All rotations are in clockwise direction in a right-handed coordinate system. For all the combinations of translation distances and rotation angles, a horizontal slice is extracted from the center of the binary volume. The size and resolution of this slice are matched to the spatially averaged ultrasound image using linear interpolation. The sum of absolute differences between the pixels in this slice and the ultrasound plane is calculated as a measure of similarity. The minimum sum of absolute differences corresponds with the combination of settings that describes the best matching slice. The algorithm is illustrated in Figure 7.

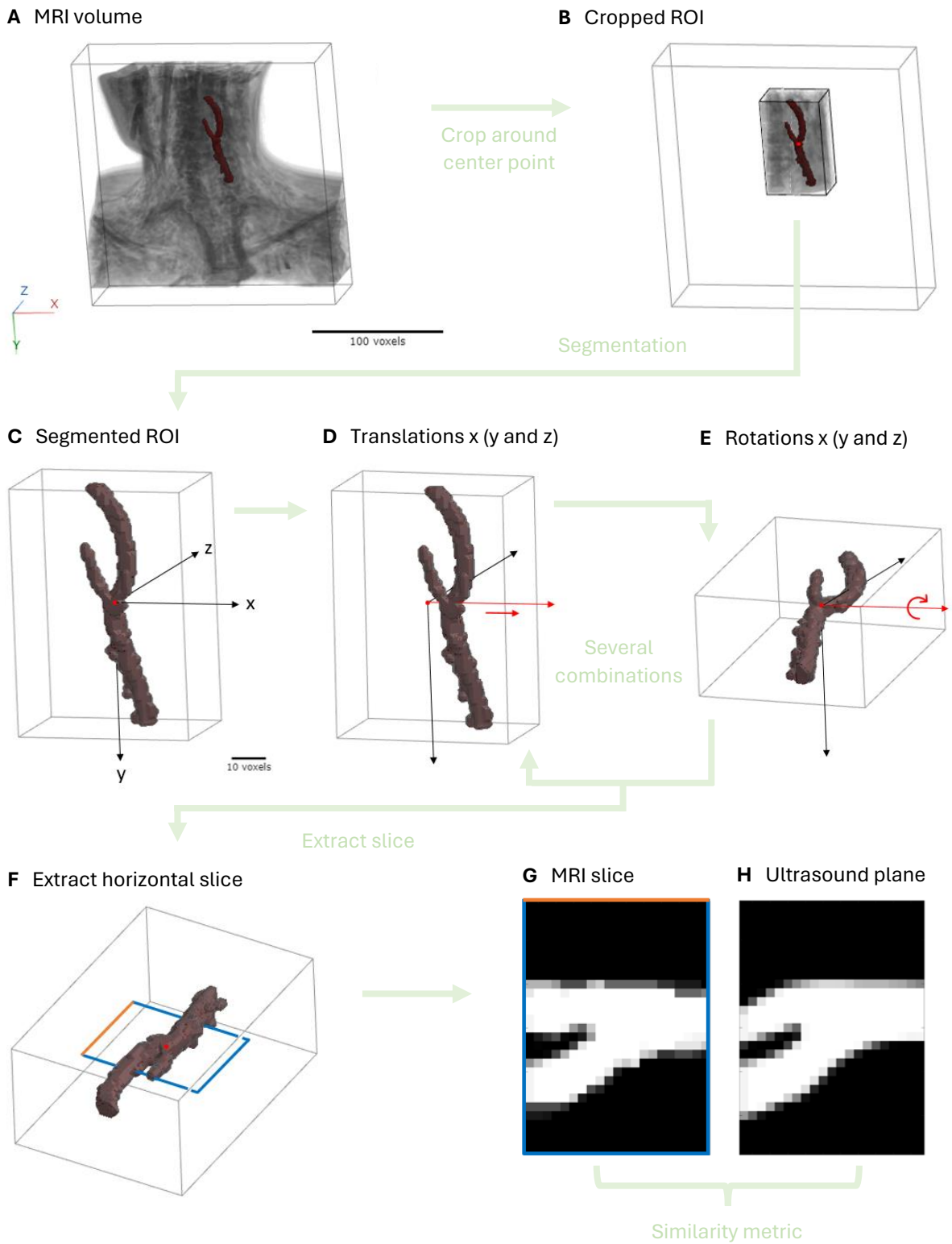

Figure 7 The search algorithm explained. The MRI volume (A) is cropped around a manually selected center point in the carotid artery bifurcation (B). The magnitude information is used to segment the carotid artery to obtain a 3D binary search volume (C). This volume is translated in the x (D), y, and z direction over varying combinations of distances and rotated around the x (E), y, and z-axis with multiple combinations of angles. From the center of the resulting volumes a horizontal plane is extracted (F). Every MRI slice (G) is then compared to the ultrasound plane (H) using the sum of absolute differences.

In practice, first a manual initialization of the MRI volume translations and rotations, of which the extracted horizontal slice is roughly comparable to the ultrasound plane, was obtained for every volunteer. Then, the algorithm was executed in two iterative steps to limit computational time. The first iteration was a quick search with a step size of 1 pixel and 2° for translation distances and rotation angles, respectively. The quick search was executed for all combinations of translations along the x, y, and z-axis from -5 to +5 pixels around their initialization, rotations around the x and y-axis from -15° to +15° around their initialization, and rotations around the z-axis from -30° to +30° around the initialization. The second iteration was a finetuning step, where the step size for the rotation angles was decreased to 1°. The boundaries for the translations and rotations of the second iteration were determined based on the outcomes of the first iteration. For each translation direction and rotation axis separately, a graph was drawn based on the found best settings which showed the influence of a change in that parameter on the sum of absolute differences of the planes. It was expected that a clear minimum sum of absolute differences would be found for the optimal combination of settings with increasing sum of absolute differences for larger deviations from these settings. If this was the case for the results of the first iteration, a limit for the sum of absolute differences was set manually and was used as a cut-off value for the boundaries of the second iteration. If again a minimum was found for the second iteration, this minimum determined the optimal combination of settings that described the orientation of the best matching slice through the 3D volume. If no minimum was found for the first or second iteration, the volunteer was excluded from further evaluation.

4.3.3 Outcome measure

Since the sum of absolute differences depends on the size of the ROI, the Structural Similarity (SSIM) index was calculated as an absolute measure of similarity of MRI slice and the ultrasound plane. This measure is calculated for each pixel relative to multiple pixels in a close neighborhood. An SSIM index of +1 indicates perfect similarity of two images, 0 indicates no similarity, and -1 means perfect anti-correlation.

4.4 Comparison of the velocity vectors

4.4.1 Pre-processing

If a matching slice was obtained, further evaluation of the correspondence between the MRI velocity data and the ultrafast ultrasound-based velocity estimates took place. First, the 3D MRI velocity vectors were projected on the 2D slice. Therefore, the three 3D volumes with the velocity information in the x, y, and z direction were translated and rotated with the optimal distances and angles. Again, the data in a horizontal slice was extracted from the center of the volume. This resulted in three datasets of the velocity magnitude in the x, y, and z direction, which together describe a 3D vector for every pixel in the slice. These vectors were projected on the axial and lateral direction of the slice in 3D to obtain the desired 2D velocity vectors.

The ultrasound velocity vectors were estimated on a grid with an approximately 12 fold higher resolution in the axial direction and 11 fold higher resolution in the lateral direction. For quantitative comparison, therefore, the ultrasound-based velocity estimates were spatially averaged to obtain velocity estimates at the same grid as MRI (29 x 21 pixels). The MRI values were masked with the ROI of ultrasound-based velocity estimates. Temporal resolution of ultrasound-based velocity vector imaging was on average 4 ± 0.5 fold higher than 4D flow MRI, varying with the difference in heart rate between ultrasound and MRI acquisitions. Therefore, temporal averaging of the ultrasound velocity estimates around the timepoint of interest was applied to obtain more comparable estimates for quantitative analysis.

4.4.2 Evaluation and outcome measures

The mean and 95% confidence interval of the temporal velocity profiles of ultrasound and MRI over one cardiac cycle (RR-interval) at three manually determined locations in the ROI, at close distances of approximately 2.4 mm from one another, were qualitatively evaluated. The temporal velocity profiles were used to redetermine more accurate matching timepoints of PSV and were shifted according to them. The mean and 95% confidence interval of the spatial velocity profiles of ultrasound and MRI over three lines across the lumen diameter of the ROI at PSV were visualized. In addition, the velocity vectors over the entire ROI at PSV were quantitatively evaluated, based on two measures of correspondence:

- The cosine similarity of the ultrasound-based velocity vectors and MRI velocity vectors at PSV was calculated, according to Equation 3.

$$Cosine\ similarity = {}^{v_{ultrasound} \cdot v_{MRI}}/_{|v_{ultrasound}||v_{MRI}|} \quad [3]$$

  Where $v_{ultrasound} \cdot v_{MRI}$ denotes the inner vector product and $|v_{ultrasound}||v_{MRI}|$ denotes the product of the velocity magnitudes. The cosine similarity is a measure of correspondence of the direction of the vectors. In other words, it indicates whether the vectors are pointing in roughly the same direction. The resulting similarity ranges from -1 to +1, where two vectors pointing in exactly the same direction (independent of their magnitudes) have a similarity of +1, two orthogonal vectors have a similarity of 0, and two opposite vectors have a similarity of -1. The cosine similarity was calculated two times: 1) for all velocity estimates and 2) only considering the reliable velocity estimates.

- The root-mean-square error (RMSE) of the correlation of axial and lateral velocity magnitudes between ultrasound and MRI at PSV were obtained for the total of 7 volunteers, according to Equation 4.

$$RMSE = \sqrt{{}^{1}/_{n} \sum_{i=1}^{n} \big(EST(i) - GT(i)\big)^2} \quad [4]$$

  With n the number of estimated samples within the ROI, $EST(i)$ the estimated value for sample i, and $GT(i)$ the ground truth value for sample i. The RMSE was used as a measure of correspondence of axial and lateral velocity magnitudes. The correlation plots were visualized.

5. Results

5.1 Cohort characteristics

A total of 20 volunteers underwent both ultrafast ultrasound imaging and 4D flow MRI. However, 5 participants were excluded for analysis with the registration algorithm either due to the absence of ECG data (n = 1), failure to obtain a clear ultrasound velocity trace with the current settings (n = 1), failure to obtain a reliable lumen segmentation on ultrasound (n = 1) or skewed acquisition of the MRI volume relative to the other participants (n = 2). During analysis with the registration algorithm, 8 additional participants were excluded, either because no reliable initialization could be determined since characteristic geometric features were missing (n = 4) or no minimum sum of absolute differences was found within the search regions (n = 4). This resulted in the inclusion of 7 volunteers for further analysis of the velocity vector comparison between ultrasound and MRI.

Of these 7 volunteers, 3 were men and 4 were women. 3 of them belonged to the age group of 20 to 30 years old and 4 belonged to the age group of 65 to 75 years old. Median [min – max] time between ultrasound and MRI measurements was 0 [0 – 7] days. Overall, median [min – max] blood pressure was 131/76 [102/62 – 158/96) mmHg and median heart rate [min – max] was 70 [51 – 86] bpm. When comparing ultrasound and MRI, median [min – max] difference between systolic and diastolic blood pressure was 55 [36 – 64] mmHg and 52 [40 – 68] mmHg and median [min – max] heart rate was 73 [56 – 86] bpm and 70 [51 – 70] bpm, respectively.

5.2 Outcomes of the registration algorithm

Median [min – max] runtime of the registration algorithm for both iterations was in total 16.3 [11.4 – 21.7] hours. An example (of volunteer 4) of the outcome of the registration algorithm, is displayed in Figure 8. The graphs show the minimum sum of absolute differences of the MRI slice and ultrasound plane at the optimal settings of translation distances and rotation angles. For each translation direction and rotation axis separately, the influence of a change in its value relative to the optimal settings on the outcome of the algorithm is shown for both iterations. The zero value is calculated as the sum of absolute differences between the ultrasound plane and a fully black MRI plane. The limit is the manually chosen cut-off value that determines the boundaries of the settings for the second iteration. It can be seen that the minimum for the sum of absolute differences is less clear for varying translations along the y-axis and rotations around the z-axis. In addition, the results of the second iteration show a sawtooth shape in the graphs of the rotation angles which hinders the reliability of the minimum. This is seen for all participants in this study.

Figure 9 shows two examples (of volunteer 4 and 7) of the best matching slice through the MRI segmentation resulting from the registration algorithm, the corresponding segmented ultrasound plane, and their overlay. The first example has good overlap, whereas the second example shows large deviations between the ROIs. In particular, there is a difference visible in the upper branch after bifurcation, the ECA. Quantitative comparison of the resulting best matching MRI slices with the ultrasound planes for all volunteers results in a median [min – max] SSIM of 0.94 [0.71 – 0.97]. The SSIM indices for all included volunteers separately are given in Table 4.

Table 4 Outcome measures for the 7 included volunteers separately

Volunteer	**1**	**2**	**3**	**4**	**5**	**6**	**7**	**Median**
SSIM	0.96	0.92	0.95	0.97	0.94	0.87	0.71	0.94
Cosine similarity all velocity vectors	0.69	0.62	0.72	0.86	0.74	0.69	0.55	0.69
Cosine similarity reliable estimates	0.79	0.71	0.76	0.87	0.83	0.68	0.77	0.77
RMSE axial velocity magnitude (cm/s)	7.84	5.34	4.43	5.99	5.78	7.60	11.03	5.99
RMSE lateral velocity magnitude (cm/s)	17.93	14.78	12.15	16.16	21.32	23.64	29.47	17.93

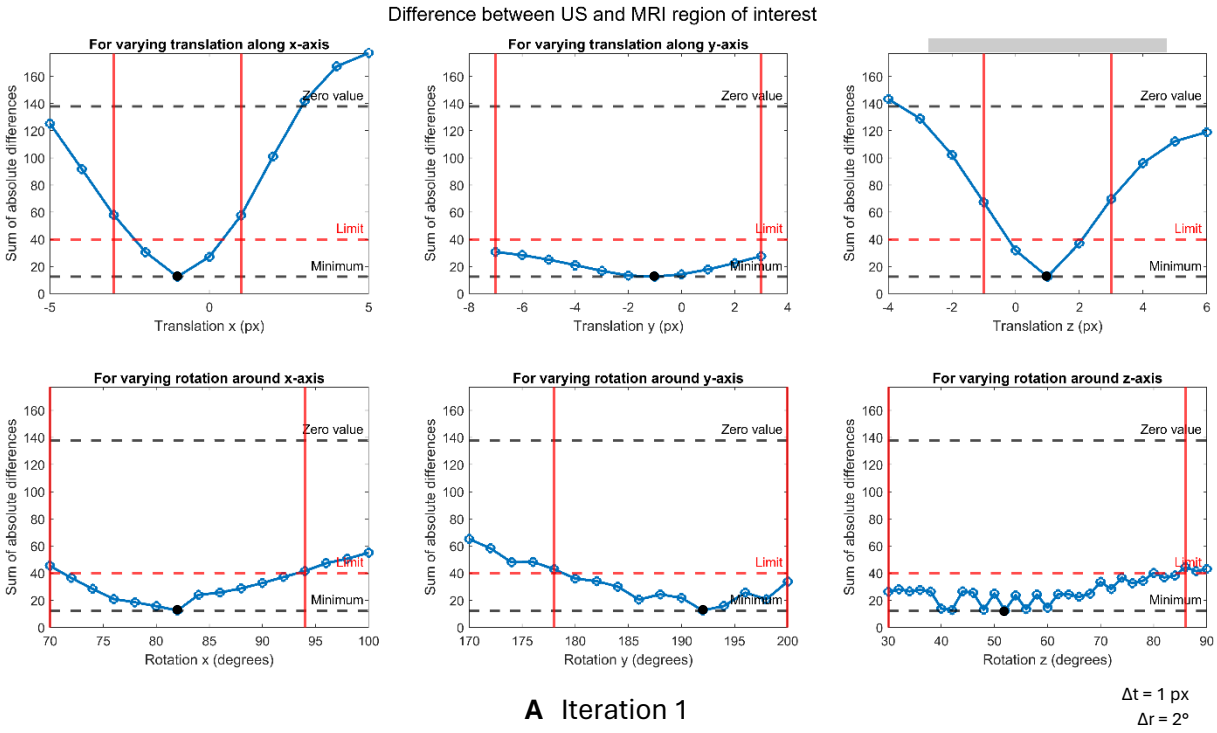

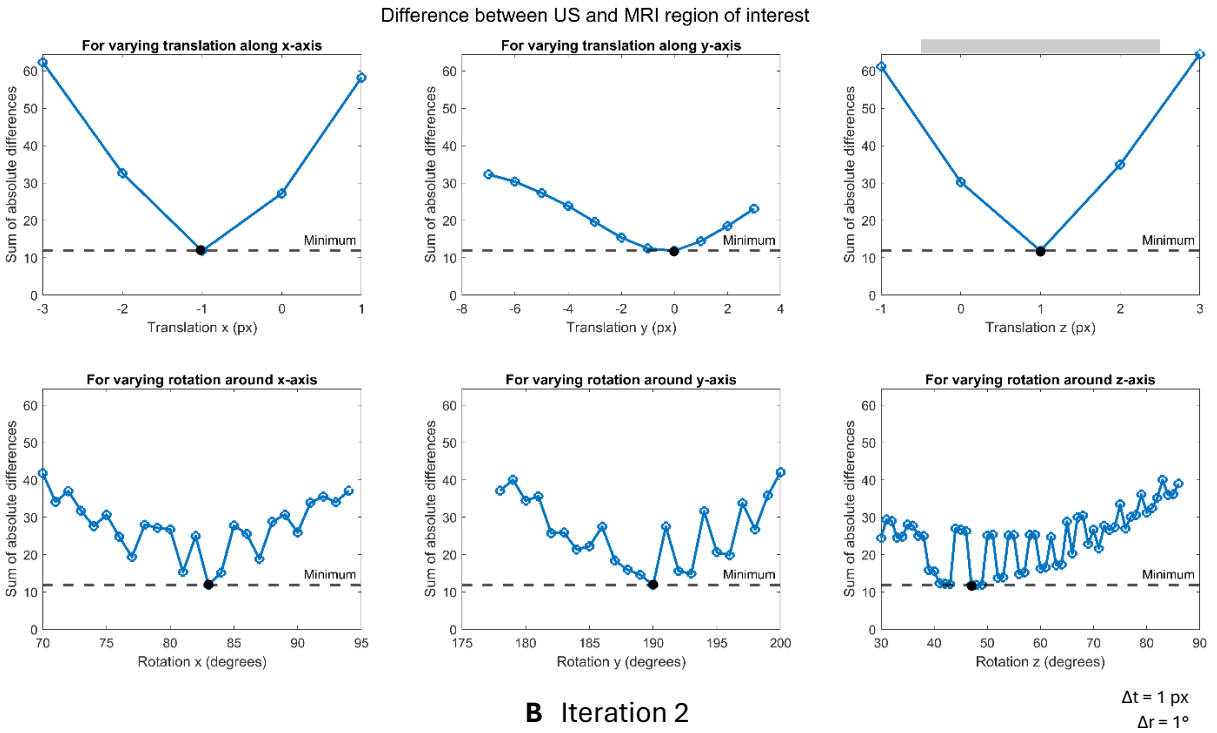

Figure 8 Example (v4) of the influence of a change in one parameter of the best match settings on the sum of absolute differences for both iterations (A and B) of the algorithm. The minimum sum of absolute differences are marked with black dots. The step sizes for the translations Δt and rotations Δr are given. The limit and zero value are visible in Iteration 1.

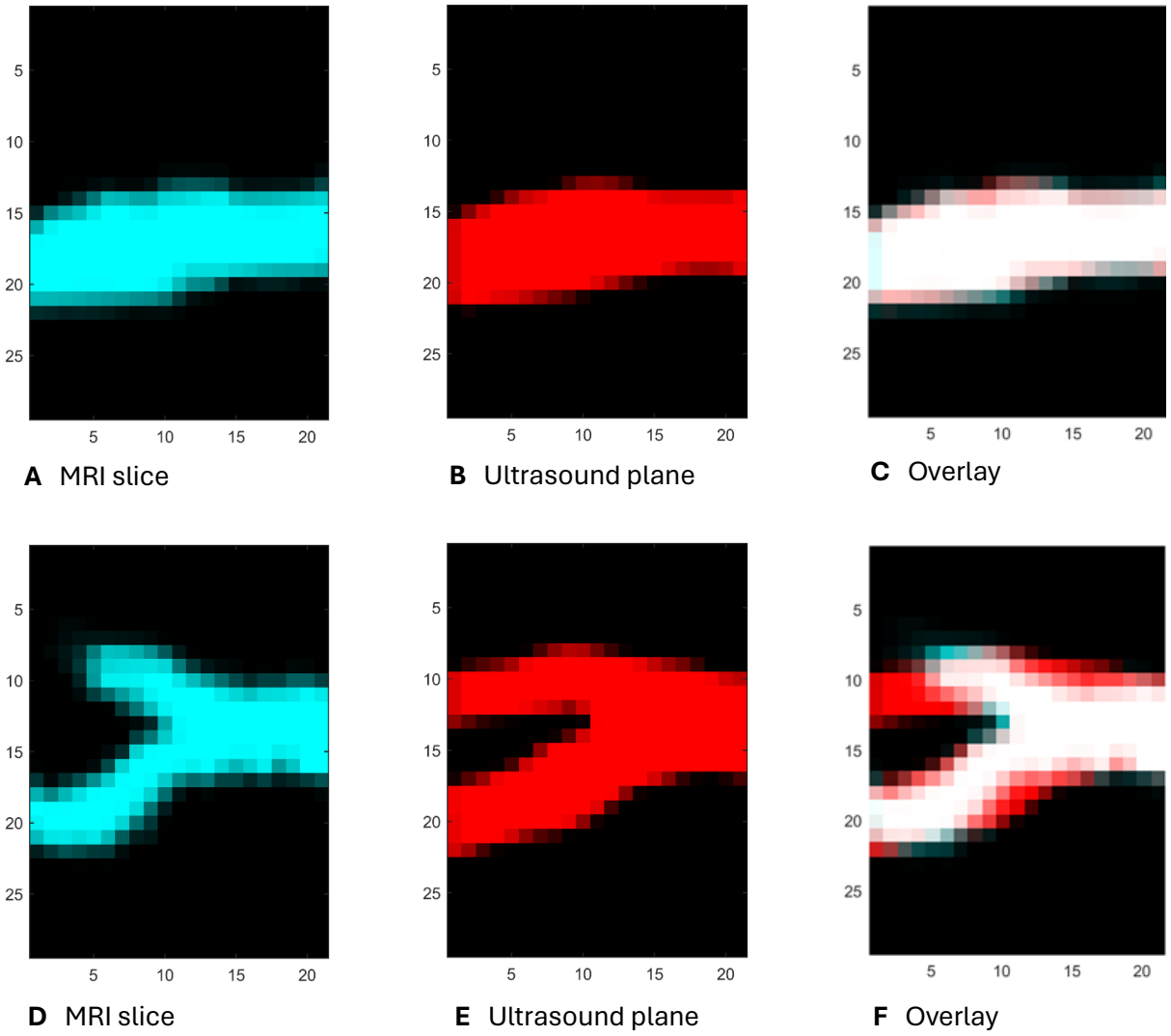

Figure 9 Two examples (v4 (top) and v7 (bottom)) of a resulting best matching slice through the MRI segmentation (A and D), the corresponding segmented ultrasound plane (B and E), and their overlay (C and F). The overlapping pixels are visualized in white.

5.3 Outcomes of the comparison of the velocity vectors

The temporal velocity profiles and spatial velocity profiles for all 7 included volunteers are given in Figure 11 and 12, respectively. The temporal velocity profiles show overall good correspondence in shape. What stands out, is the fact that there is a difference in the duration of one cardiac cycle between ultrasound and MRI acquisitions for multiple participants. This complicates the comparison over time. There are differences in maximum velocity measured with both modalities for some volunteers. Yet, these differences are not consistently larger or smaller for one modality relative to the other. Likewise, the spatial velocity profiles show good correspondence between ultrasound and MRI with small varying deviations in maximum velocity. The spatial velocities show a more or less laminar flow profile, as expected.

Two examples (of volunteer 4 and 7) of an overlay of the reliable velocity vectors of MRI (blue) and spatially averaged ultrasound (red) over the full ROI at PSV are depicted in Figure 10. The reliable velocity vectors of the first example seem to match really well by eye. However, in the second example deviations in direction and size of the velocity vectors are visible, especially in the two branches of the ROI after bifurcation. From these overlays, the cosine similarity is calculated for all included volunteers. This results in a median [min – max] cosine similarity for all velocity vectors of 0.69 [0.55 – 0.86]. When considering only the reliable velocity vectors, the median [min – max] cosine similarity becomes 0.77 [0.68 – 0.87]. The cosine similarity values for all included volunteers separately are given in Table 4.

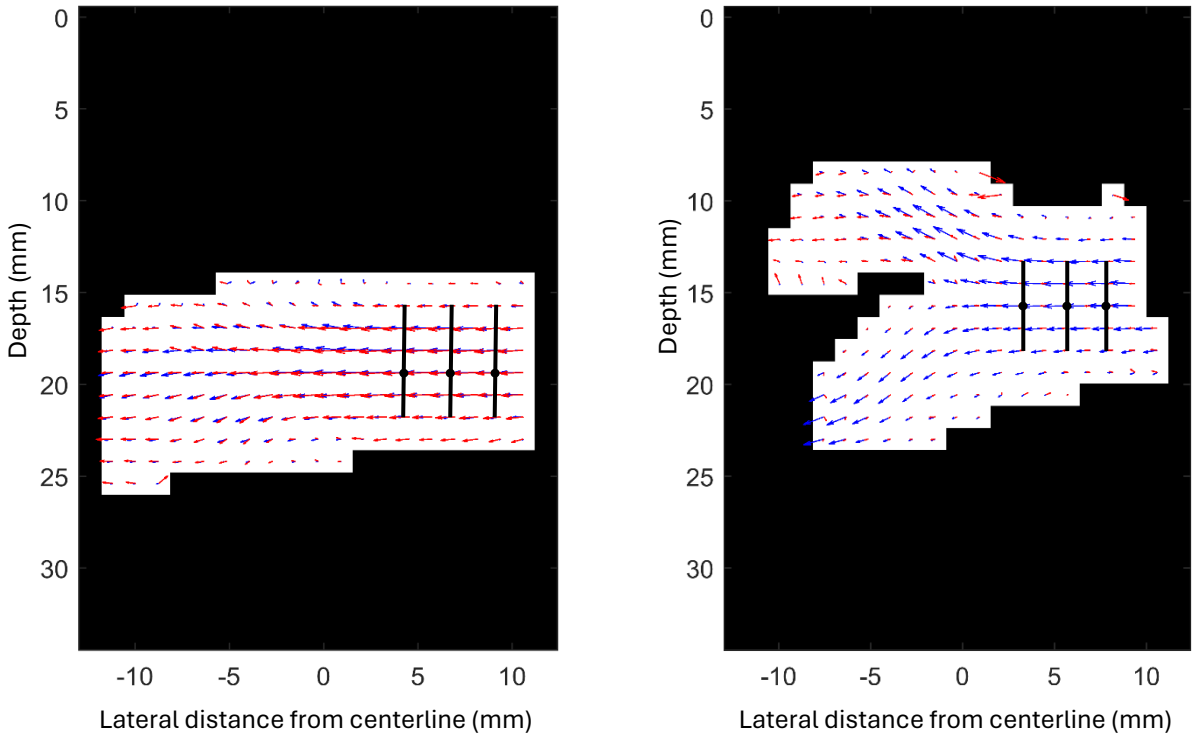

Figure 10 Two examples (v4 (left) and v7 (right)) of an overlay of the reliable velocity vectors of MRI (blue) and spatially averaged ultrasound (red) at PSV with the locations of the temporal and spatial velocity profiles marked with black dots and stripes, respectively.

The correlation plots of the axial and lateral velocities of MRI and spatially averaged ultrasound at PSV taken together for all included participants are shown in Figure 13. Both the axial velocity and lateral velocity magnitude show a positive correlation between MRI and spatially averaged ultrasound. However, the lateral velocity magnitude shows a stronger correlation between MRI and ultrasound measurements than the axial velocity magnitude. The absolute RMSE for axial and lateral velocity magnitudes are 7.32 cm/s and 20.44 cm/s, respectively. The absolute axial and lateral RMSE values for all included volunteers separately are set out in Table 4.

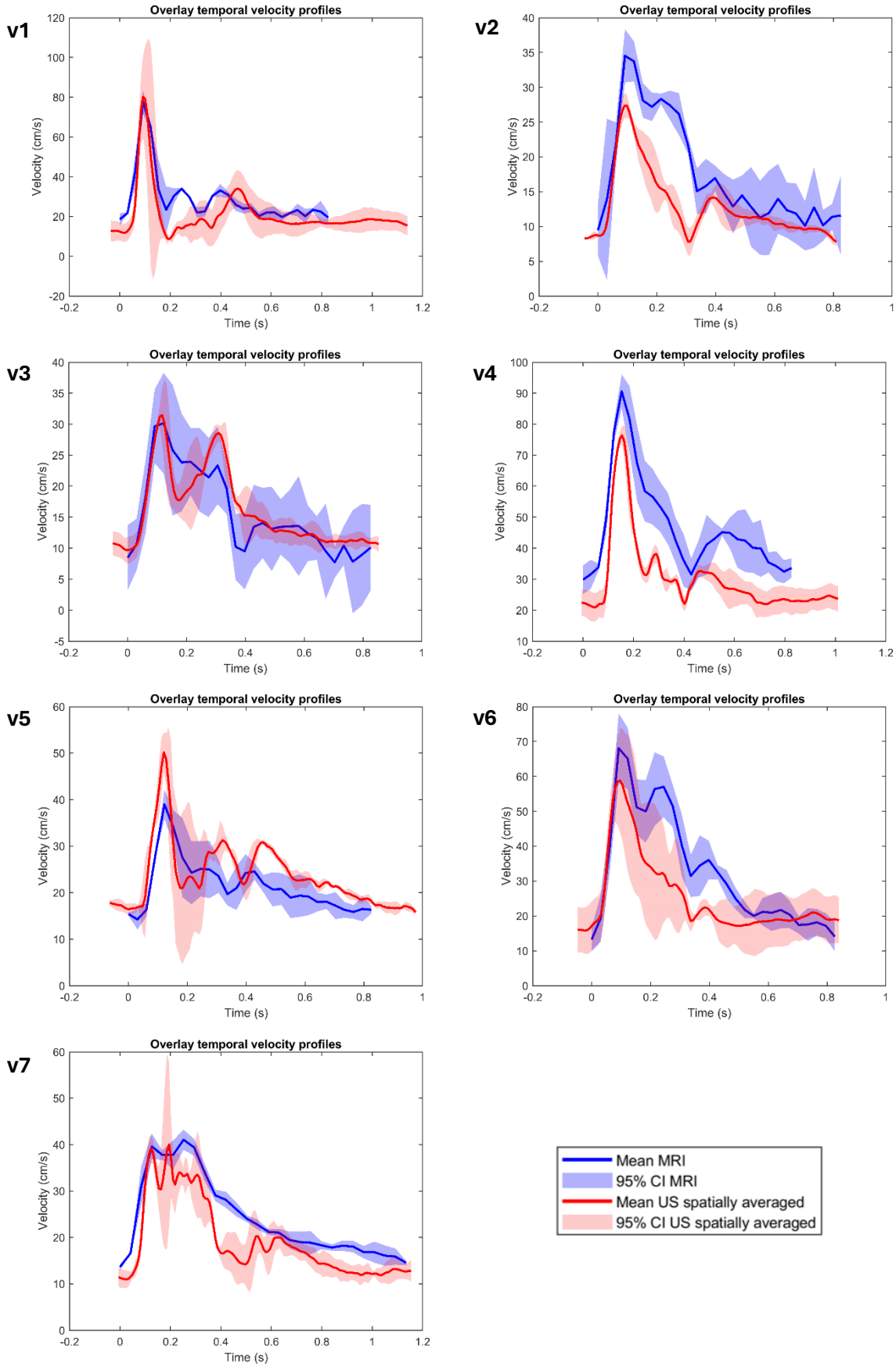

Figure 11 Mean temporal velocity profiles and their 95% confidence interval of MRI (blue) and spatially averaged ultrasound (red) for all included volunteers (v1 t/m v7).

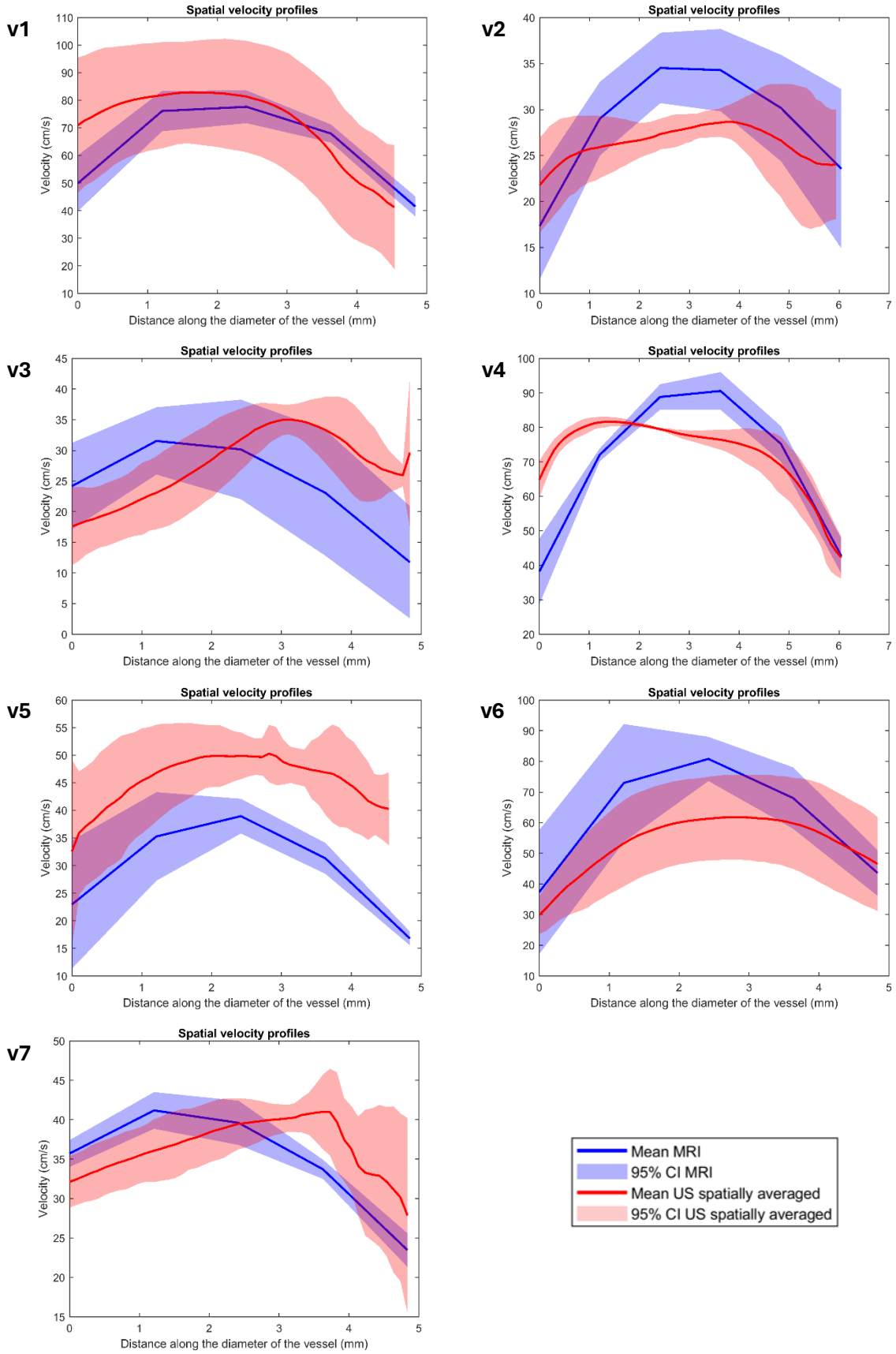

Figure 12 Mean spatial velocity profiles and their 95% confidence interval of MRI (blue) and spatially averaged ultrasound (red) at PSV for all included volunteers (v1 t/m v7). Unreliable ultrasound velocity estimates are not visualized.

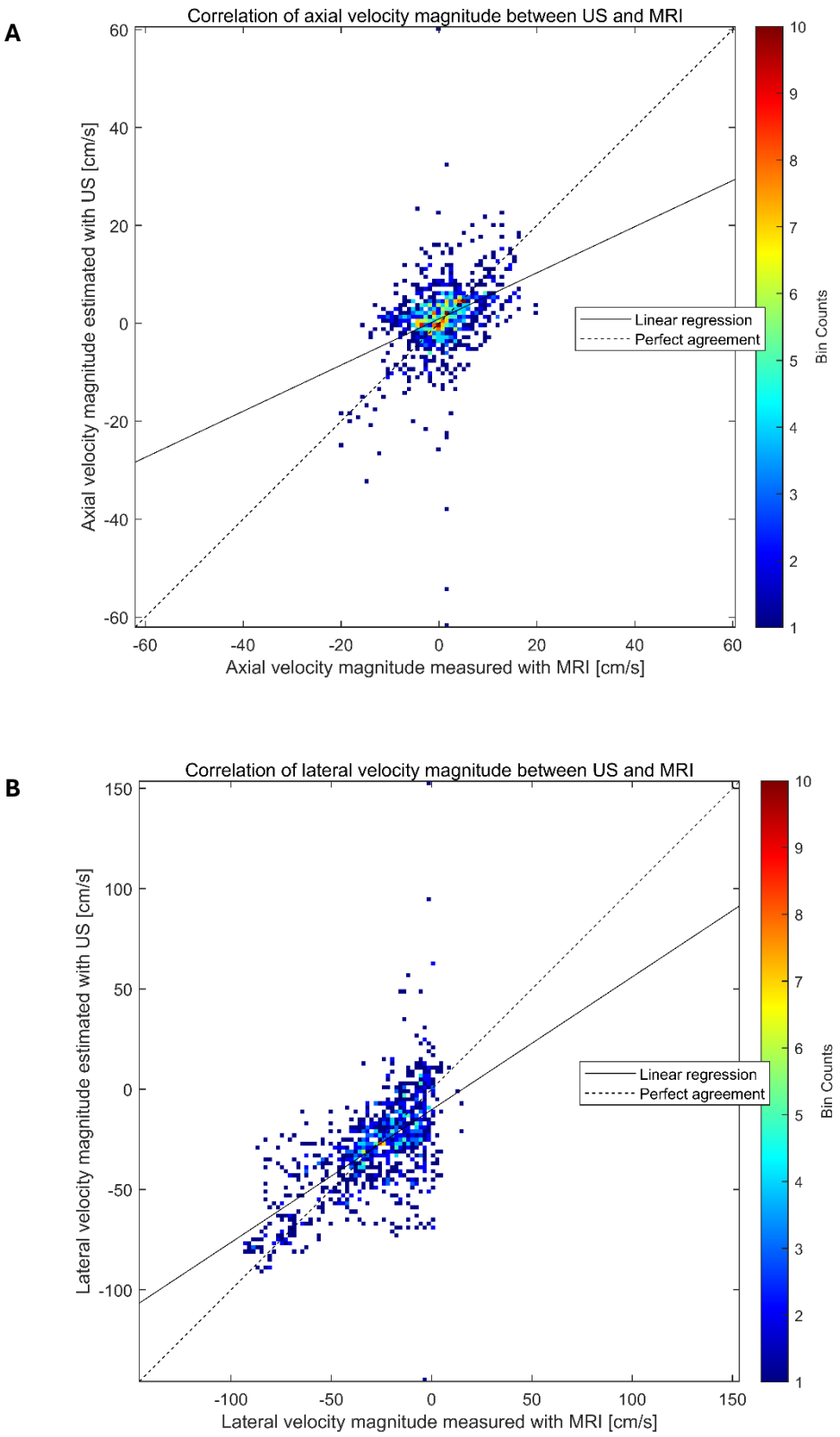

Figure 13 Correlation plots of the axial (A) and lateral (B) velocity magnitudes of MRI and spatially averaged ultrasound at PSV for all 7 volunteers together.

6. Discussion

This chapter describes the interpretation of the results, the limitations of the study, and recommendations for future research.

6.1 Interpretation of the results

In this work, an algorithm for registration of 3D MRI to 2D ultrasound based on geometrical information is presented. Although the algorithm found a slice through the MRI volume that matches to the ultrasound plane for 7 volunteers, the reliability of the positioning of these slices is up for debate. The minimum sum of absolute differences is uncertain, mainly for translations in the y-direction and rotations around the z-axis, as can be seen in Figure 8. This is most likely a consequence of the low resolution of the MRI scan and the dependent spatial averaging of the ultrasound ROI. The low resolution results in the smoothing of characteristic geometric features of the carotid artery, like the carotid bulb, thereby limiting the information that is available for registration. The carotid segmentations on MRI and ultrasound appear in many cases as straight tubes. A displacement in the longitudinal direction (y-direction) of a 'straight tube' or a rotation around its longitudinal axis (the z-axis, after rotations of the volume around the x and y-axis), has a much smaller effect on the sum of absolute differences than a displacement in any other direction or a rotation around any other axis. Presumably, the low resolution of the MRI scan is also the cause for the sawtooth pattern which can be seen in the graphs of the rotations of the second iteration of the algorithm in Figure 8. A step size of 1° for the rotations, results in a maximum shift of the outer pixels of the plane of approximately $^{35}/_{2} \cdot \tan 1^\circ = 0.3$ mm. This shift is around 4 times smaller than the resolution of the MRI scan, meaning the variation in the sum of absolute differences at this level is a result of the interpolation between pixels rather than the selection of pixels in a different slice. In other words, the search for the matching slice is executed with an accuracy larger than the resolution of the MRI scan. For future research, it is recommended to run the algorithm with a step size that is adjusted to the resolution of the data. For this study, this means a minimum step size for the rotations of approximately 4°. An additional advantage of this is the possibility to run the algorithm for a broader search region in less time. It can be considered to allow for some interpolation between pixels by using a smaller step size, as long as no sawtooth pattern occurs and a clear minimum sum of absolute differences is ensured. Alternatively, the fitting of a parabolic curve may be taken into consideration to determine the overall minimum sum of absolute differences.

The found matching planes show relatively high SSIM indices for all included volunteers with a median [min – max] of 0.94 [0.71 – 0.97]. However, the plane through the MRI segmentation, the corresponding segmented ultrasound plane, and their overlay for volunteer 7 show a clear deviation in the ECA branch, as depicted in Figure 9D t/m F. From this result, it can be concluded that the anatomy of the carotid artery and the orientation of the ICA and ECA relative to each other have changed between ultrasound and MRI measurements for this volunteer. Alterations in the anatomy may have complicated the registration for some of the other volunteers as well. Presumably, the SSIM index is quite high for all volunteers due to the many black pixels outside the ROI that are taken into account for the similarity metric as well. For future research, it may be more meaningful to implement a similarity metric that focuses solely on the ROI.

The uncertainty and deviations in the registration of MRI to ultrasound affect the reliability of the outcomes of the comparison of the velocity vectors. Any dissimilarity found between the velocity vectors of MRI and ultrasound can be a consequence of an inaccurately positioned plane instead of incorrect velocity vectors. This has to be kept in mind for the interpretation of the results from the comparison of the velocity vectors.

When comparing temporal velocity profiles between ultrasound and MRI in Figure 11, the shapes of the profiles match quite well for all included volunteers. The maximum velocities measured with MRI and ultrasound may differ a little, but no consistent, systematic error is found. The same applies to the spatial velocity profiles of ultrasound and MRI in Figure 12. In general their shapes correspond well and show laminar flow, but the maximum velocities may deviate a little. Notable is the fact that for temporal and spatial velocity profiles of 4 volunteers (v2, v3, v5, and v7) the maximum velocities of both ultrasound and MRI measurements do not exceed 50 cm/s, whereas normative velocities in the CCA and ICA are on average 88.7 ± 20.2 and 80.3 ± 18.0 cm/s, respectively. [35] For two of them (v2 and v3), also lower maximum velocities were measured with conventional Doppler ultrasound.

The cosine similarity for all velocity estimates as well as incorporating only the reliable ultrasound and corresponding MRI estimates is quite high with a median [min – max] of 0.69 [0.55 – 0.86] and 0.77 [0.68 – 0.87], respectively. This means that the vectors are pointing in roughly the same direction. The absolute RMSE for the axial and lateral velocities of all volunteers taken together are 7.32 cm/s and 20.44 cm/s, respectively. These errors are hard to interpret, since they are sensitive to outliers and depend on the range of data that they are derived from. Multiple outliers can be seen in Figure 13 for both axial and lateral ultrasound velocity magnitudes corresponding to MRI velocity magnitudes around 0 cm/s. The axial velocity magnitudes range from 0 to 20.32 cm/s for MRI, resulting in a percentual error of approximately 36%. The lateral velocity magnitudes range from 0 to 93.46 cm/s for MRI, resulting in a percentual error of approximately 22%. These RMSE values seem quite high. However, similar absolute RMSE values were described by Saris *et al.* [27] for axial and lateral velocity components obtained with the compound speckle tracking technique in comparison to true velocity components in FIELD II simulations of physiological flow at a PRF of 12 kHz. Furthermore, they showed that the RMSE values are increasing around the peak systolic phase. Thus, it would be expected that the RMSE of axial and lateral velocity magnitudes in this study would also decrease for different phases during the cardiac cycle.

6.2 Limitations of the study

There are several limitations of this study, of which the most important ones are discussed hereafter.

Firstly, there are a lot of manual steps in this algorithm that influence the results. For example, the thresholding of the MRI scan using the triangle method results for some scans in an inaccurate segmentation where noise and/or closely running veins are also segmented. The manual adjustments performed in these segmentations may have an influence on the outcome of the registration algorithm. It could be valuable to investigate the performance of other segmentation techniques. For example, it might be worth trying to reconstruct a phase contrast MR angiography from the voxelwise multiplication of magnitude data and absolute velocities, like Aalbregt *et al.* [36] did. Besides, the initialization of the registration algorithm, the choice for MRI volume translations and rotations of which the extracted horizontal slice is roughly comparable to the ultrasound plane, is performed manually. A wrong initialization could result in the finding of a local minimum using the registration algorithm. To minimize this chance, it was chosen in this study to exclude volunteers for which an initialization could not be determined with certainty. The arrival of new functions in MATLAB (R2023a, MathWorks, Natick, Massachusetts, USA) to show volumes in 3D and interactively position a clipping plane in them, may expand the options for easier and more accurate initialization in future studies. Furthermore, the temporal velocity

profiles are derived from one or more manually chosen locations in the ROI, during pre-processing of the data for the registration algorithm and again for obtaining the outcome measures for comparison of the velocity vectors. The timepoint and phase of PSV for ultrasound and MRI vary over the ROI. Thus, the manual indication of a location for the temporal velocity profiles may have an impact on the outcomes.

Secondly, the temporal velocity profiles of MRI and ultrasound of most participants show a difference in the duration of one cardiac cycle due to a difference in heart rate. This has complicated the implementation of temporal matching of MRI and ultrasound over a full cardiac cycle and has forced matching only at PSV for MRI and ultrasound. However, during systole often complex blood flow occurs which is difficult to track in 2D. Therefore, it would be informative to perform comparison at several other timepoints during the cardiac cycle in future research.

Thirdly, it is expected that data of ultrasound and MRI is compared for quite different situations in some volunteers, due to the relatively long time between ultrasound and MRI measurements and a possible difference in neck position during measurements. The neck is highly mobile, therefore the anatomy of the carotid artery may have changed between measurements. The fact that there is no ground truth information about the position in space of the plane that is acquired with ultrasound, makes it difficult to determine how well the registration algorithm functions.

And lastly, but most importantly, 4D flow MRI has its own downsides, including a much lower temporal and spatial resolution than ultrafast ultrasound-based velocity vector imaging and the averaging of acquisitions at specified phases during the cardiac cycle over multiple heartbeats. In this study, the ultrafast ultrasound-based velocity vectors are spatially and temporally averaged to allow for comparison. Nevertheless, it remains difficult to prove the benefits of ultrafast ultrasound-based velocity vector imaging, like the higher temporal and spatial resolution which enable the visualization of short-lived events that underlie complex blood flow. Zooming in on complex blood flow patterns in patient ultrasound data and comparing them to the MRI data, may be a first step in future research to prove the benefit of ultrafast ultrasound-based velocity vector imaging.

6.3 Recommendations for future research

Comparison studies of ultrasound to 4D flow MRI by Harloff *et al.* [37], Engelhard *et al.* [38], and Han *et al.* [39], all use manual positioning of a plane in the 3D MRI volume to compare to ultrasound. To the best of our knowledge, this study is new in the way that it uses a semi-automatic algorithm for the registration of 4D flow MRI to ultrafast ultrasound. Although the registration algorithm does not function optimally yet and requires further development, we see benefit in the quantitative insight it gives in the accuracy of its optimal registration relative to slightly different registrations. In addition to the recommendations previously described, a few important recommendations for future research to improve the registration algorithm and the outcomes are described hereafter.

Firstly, it would be highly recommended to add a high resolution anatomical MRI scan and ECG-recording to the scanning protocol, which can be used for improved spatial and temporal registration. Besides, it might be worth looking into mutual information as a similarity metric, since it is often used as a metric for registration of multimodal images. [40] However, keep in mind that the use of information from surrounding veins or other structures might be counterproductive in some cases, as the anatomy is very variable with movement.

In addition, the robustness of the algorithm must be tested to give answers to important questions, like ‘what is the effect of a slightly different registration of the MRI volume to the ultrasound plane on the outcomes of the comparison of the velocity vectors?’ And ‘how do the outcomes of the registration algorithm compare to the outcomes of the manual initialization?’ This may give insight in the efficacy and added value of a semi-automatic registration algorithm.

This study is a first step towards the in vivo validation of ultrafast ultrasound-based velocity vector imaging, which can have major implications for patient-specific risk assessment of vascular disease and indications for interventions. Already several patient studies are ongoing at the Rijnstate hospital, Arnhem, the Netherlands, and at the Radboud University Medical Center, Nijmegen, the Netherlands, to investigate the influence of flow parameters, like WSS, vorticity, and vector complexity calculated from ultrafast ultrasound-based velocity vector data, on progression and rupture of atherosclerotic plaques in the carotid artery. These studies are the next step in proving the added value of the use of ultrafast ultrasound-based velocity vector imaging in clinical practice.

7. Conclusion

To conclude, this study is a first step towards the in vivo validation of ultrafast ultrasound-based velocity vector imaging using blood speckle tracking in the carotid artery of healthy volunteers against 4D flow MRI. A semi-automatic algorithm was proposed for the registration of MRI to ultrasound, which requires further development and evaluation. The ultrasound velocity vector estimates show overall fairly good agreement with the MRI data, but more extensive evaluation is needed. Nonetheless, this study underwrites the great potential of ultrafast ultrasound-based velocity vector imaging to contribute to patient-specific risk assessment of vascular disease and more accurate indications for interventions in future clinical practice.

Bibliography

[1] V. L. Feigin *et al.*, “World Stroke Organization (WSO): Global Stroke Fact Sheet 2022,” *International Journal of Stroke*, vol. 17, no. 1, pp. 18–29, Jan. 2022, doi: 10.1177/17474930211065917.

[2] V. L. Feigin *et al.*, “Global, regional, and national burden of stroke and its risk factors, 1990-2019: a systematic analysis for the Global Burden of Disease Study 2019,” *Lancet Neurol*, vol. 20, no. 10, pp. 1–26, 2021, doi: 10.1016/S1474-4422(21)00252-0.

[3] V. Aboyans *et al.*, “2017 ESC Guidelines on the Diagnosis and Treatment of Peripheral Arterial Diseases, in collaboration with the European Society for Vascular Surgery (ESVS),” *Eur Heart J*, vol. 39, no. 9, pp. 763–816, Mar. 2018, doi: 10.1093/EURHEARTJ/EHX095.

[4] Nederlandse Vereniging voor Neurologie, “Richtlijn - Herseninfarct en hersenbloeding,” Richtlijnendatabase Federatie Medisch Specialisten. Accessed: Feb. 10, 2023. [Online]. Available: https://richtlijnendatabase.nl/richtlijn/herseninfarct_en_hersenbloeding/startpagina_herseninfarct_-bloeding.html

[5] Nederlandse Vereniging voor Non-Invasieve Vaatdiagnostiek, “Richtlijn duplexonderzoek van de carotiden.” Accessed: Feb. 21, 2023. [Online]. Available: https://www.vnivd.nl/upload/duplexonderzoek-van-de-carotiden.pdf

[6] S. F. Cheng *et al.*, “The 2nd European Carotid Surgery Trial (ECST-2): rationale and protocol for a randomised clinical trial comparing immediate revascularisation versus optimised medical therapy alone in patients with symptomatic and asymptomatic carotid stenosis at low to intermediate risk of stroke,” *Trials*, vol. 23, no. 1, Dec. 2022, doi: 10.1186/S13063-022-06429-Z.

[7] P. M. Rothwell *et al.*, “Analysis of pooled data from the randomised controlled trials of endarterectomy for symptomatic carotid stenosis,” *The Lancet*, vol. 361, no. 9352, pp. 107–116, Jan. 2003, doi: 10.1016/S0140-6736(03)12228-3.

[8] L. Karlsson *et al.*, “Risk of Recurrent Stroke in Patients with Symptomatic Mild (20–49% NASCET) Carotid Artery Stenosis,” *European Journal of Vascular and Endovascular Surgery*, vol. 52, no. 3, pp. 287–294, Sep. 2016, doi: 10.1016/J.EJVS.2016.05.014.

[9] Y. Du *et al.*, “Wall Shear Stress Measurements Based on Ultrasound Vector Flow Imaging: Theoretical Studies and Clinical Examples,” *J Ultrasound Med*, vol. 39, no. 8, pp. 1649–1664, Aug. 2020, doi: 10.1002/JUM.15253.

[10] J. J. Wentzel, Y. S. Chatzizisis, F. J. H. Gijsen, G. D. Giannoglou, C. L. Feldman, and P. H. Stone, “Endothelial shear stress in the evolution of coronary atherosclerotic plaque and vascular remodelling: current understanding and remaining questions,” *Cardiovasc Res*, vol. 96, no. 2, pp. 234–243, Nov. 2012, doi: 10.1093/CVR/CVS217.

[11] S. Ebrahimi and F. Fallah, “Investigation of coronary artery tortuosity with atherosclerosis: A study on predicting plaque rupture and progression,” *Int J Mech Sci*, vol. 223, p. 107295, Jun. 2022, doi: 10.1016/J.IJMECSCI.2022.107295.

[12] J. Baun, “Emerging Technology: Ultrasound Vector Flow Imaging—A Novel Approach to Arterial Hemodynamic Quantification,” *Journal of Diagnostic Medical Sonography*, vol. 37, no. 6, pp. 599–606, Nov. 2021, doi: 10.1177/87564793211036013.

[13] B. Y. S. Yiu, S. S. M. Lai, and A. C. H. Yu, “Vector projectile imaging: time-resolved dynamic visualization of complex flow patterns,” *Ultrasound Med Biol*, vol. 40, no. 9, pp. 2295–2309, 2014, doi: 10.1016/J.ULTRASMEDBIO.2014.03.014.

[14] O. Villemain *et al.*, “Ultrafast Ultrasound Imaging in Pediatric and Adult Cardiology: Techniques, Applications, and Perspectives,” *JACC Cardiovasc Imaging*, vol. 13, no. 8, pp. 1771–1791, Aug. 2020, doi: 10.1016/J.JCMG.2019.09.019.

[15] A. Bulum *et al.*, “Contribution of UltraFast; Ultrasound and Shear Wave Elastography in the Imaging of Carotid Artery Disease,” *Diagnostics 2022, Vol. 12, Page 1168*, vol. 12, no. 5, p. 1168, May 2022, doi: 10.3390/DIAGNOSTICS12051168.

[16] A. E. C. M. Saris, H. H. G. Hansen, S. Fekkes, J. Menssen, M. M. Nillesen, and C. L. de Korte, “In Vivo Blood Velocity Vector Imaging Using Adaptive Velocity Compounding in the Carotid Artery Bifurcation,” *Ultrasound Med Biol*, vol. 45, no. 7, pp. 1691–1707, Jul. 2019, doi: 10.1016/J.ULTRASMEDBIO.2019.03.008.

[17] C. D. Lew, M. T. Alley, R. Bammer, D. M. Spielman, and F. P. Chan, “Peak Velocity and Flow Quantification Validation for Sensitivity-Encoded Phase-Contrast MR Imaging,” *Acad Radiol*, vol. 14, no. 3, p. 258, Mar. 2007, doi: 10.1016/J.ACRA.2006.11.008.

[18] P. Dyverfeldt *et al.*, “4D flow cardiovascular magnetic resonance consensus statement,” *Journal of Cardiovascular Magnetic Resonance*, vol. 17, no. 1, pp. 1–19, Aug. 2015, doi: 10.1186/S12968-015-0174-5/TABLES/3.

[19] G. Montaldo, M. Tanter, J. Bercoff, N. Benech, and M. Fink, “Coherent plane-wave compounding for very high frame rate ultrasonography and transient elastography,” *IEEE Trans Ultrason Ferroelectr Freq Control*, vol. 56, no. 3, pp. 489–506, Mar. 2009, doi: 10.1109/TUFFC.2009.1067.

[20] J. Bercoff, “Ultrafast Ultrasound Imaging,” in *Ultrasound Imaging - Medical Applications*, IntechOpen, 2011. doi: 10.5772/19729.

[21] I. K. Ekroll and J. Avdal, “Adaptive clutter filtering based on tissue vector velocities,” *IEEE International Ultrasonics Symposium, IUS*, Oct. 2017, doi: 10.1109/ULTSYM.2017.8092049.

[22] A. E. C. M. Saris, “Blood velocity vector imaging in the carotid artery using ultrasound,” Radboud University Medical Center, Nijmegen, 2019.

[23] A. C. H. Yu and L. Lovstakken, “Eigen-based clutter filter design for ultrasound color flow imaging: a review,” *IEEE Trans Ultrason Ferroelectr Freq Control*, vol. 57, no. 5, pp. 1096–1111, May 2010, doi: 10.1109/TUFFC.2010.1521.

[24] I. K. Ekroll, A. Swillens, P. Segers, T. Dahl, H. Torp, and L. Lovstakken, “Simultaneous quantification of flow and tissue velocities based on multi-angle plane wave imaging,” *IEEE Trans Ultrason Ferroelectr Freq Control*, vol. 60, no. 4, pp. 727–738, 2013, doi: 10.1109/TUFFC.2013.2621.

[25] J. Jensen, C. A. V. Hoyos, M. B. Stuart, C. Ewertsen, M. B. Nielsen, and J. A. Jensen, “Fast Plane Wave 2-D Vector Flow Imaging Using Transverse Oscillation and Directional Beamforming,” *IEEE Trans Ultrason Ferroelectr Freq Control*, vol. 64, no. 7, pp. 1050–1062, Jul. 2017, doi: 10.1109/TUFFC.2017.2693403.

[26] J. Kortbek and J. A. Jensen, “Estimation of velocity vector angles using the directional cross-correlation method,” *IEEE Trans Ultrason Ferroelectr Freq Control*, vol. 53, no. 11, pp. 2036–2049, Nov. 2006, doi: 10.1109/TUFFC.2006.144.

[27] A. E. C. M. Saris, H. H. G. Hansen, S. Fekkes, M. M. Nillesen, M. C. M. Rutten, and C. L. De Korte, “A Comparison Between Compounding Techniques Using Large Beam-Steered Plane Wave Imaging for Blood Vector Velocity Imaging in a Carotid Artery Model,” *IEEE Trans Ultrason Ferroelectr Freq Control*, vol. 63, no. 11, pp. 1758–1771, Nov. 2016, doi: 10.1109/TUFFC.2016.2606565.

[28] S. Fadnes, I. K. Ekroll, S. A. Nyrnes, H. Torp, and L. Lovstakken, “Robust angle-independent blood velocity estimation based on dual-angle plane wave imaging,” *IEEE Trans Ultrason Ferroelectr Freq Control*, vol. 62, no. 10, pp. 1757–1767, Oct. 2015, doi: 10.1109/TUFFC.2015.007108.

[29] Z. Stankovic, B. D. Allen, J. Garcia, K. B. Jarvis, and M. Markl, “4D flow imaging with MRI,” *Cardiovasc Diagn Ther*, vol. 4, no. 2, p. 173, 2014, doi: 10.3978/J.ISSN.2223-3652.2014.01.02.

[30] M. Markl, A. Frydrychowicz, S. Kozerke, M. Hope, and O. Wieben, “4D flow MRI,” *Journal of Magnetic Resonance Imaging*, vol. 36, no. 5, pp. 1015–1036, Nov. 2012, doi: 10.1002/JMRI.23632.

[31] D. T. Wymer, K. P. Patel, W. F. Burke, and V. K. Bhatia, “Phase-contrast MRI: Physics, techniques, and clinical applications,” *Radiographics*, vol. 40, no. 1, pp. 122–140, Jan. 2020, doi: 10.1148/RG.2020190039/ASSET/IMAGES/MEDIUM/RG.2020190039.FIG20.GIF.

[32] L. S. Fridericia, “The Duration of Systole in an Electrocardiogram in Normal Humans and in Patients with Heart Disease,” *Annals of Noninvasive Electrocardiology*, vol. 8, no. 4, p. 343, Oct. 2003, doi: 10.1046/J.1542-474X.2003.08413.X.

[33] M. El-Segaier, O. Lilja, S. Lukkarinen, L. Sörnmo, R. Sepponen, and E. Pesonen, “Computer-based detection and analysis of heart sound and murmur,” *Ann Biomed Eng*, vol. 33, no. 7, pp. 937–942, Jul. 2005, doi: 10.1007/S10439-005-4053-3.

[34] G. W. Zack, W. E. Rogers, and S. A. Latt, “Automatic measurement of sister chromatid exchange frequency,” *J Histochem Cytochem*, vol. 25, no. 7, pp. 741–753, 1977, doi: 10.1177/25.7.70454.

[35] Y. Nagai, M. K. Kemper, C. J. Earley, and E. J. Metter, “Blood-flow velocities and their relationships in carotid and middle cerebral arteries,” *Ultrasound Med Biol*, vol. 24, no. 8, pp. 1131–1136, Oct. 1998, doi: 10.1016/S0301-5629(98)00092-1.

[36] E. Aalbregt *et al.*, “Four-Dimensional Flow MRI-Derived Hemodynamics in Abdominal Aortic Aneurysms: Reproducibility and Associations With Diameter, Intraluminal Thrombus Volume, and Vorticity,” *J Magn Reson Imaging*, Nov. 2023, doi: 10.1002/JMRI.29138.

[37] A. Harloff, T. Zech, F. Wegent, C. Strecker, C. Weiller, and M. Markl, “Comparison of blood flow velocity quantification by 4D flow MR imaging with ultrasound at the carotid bifurcation,” *AJNR Am J Neuroradiol*, vol. 34, no. 7, pp. 1407–1413, Jul. 2013, doi: 10.3174/AJNR.A3419.

[38] S. Engelhard *et al.*, “High-Frame-Rate Contrast-enhanced US Particle Image Velocimetry in the Abdominal Aorta: First Human Results,” *https://doi.org/10.1148/radiol.2018172979*, vol. 289, no. 1, pp. 119–125, Jul. 2018, doi: 10.1148/RADIOL.2018172979.

[39] Y. Han *et al.*, “Validation of Left Ventricular High Frame Rate Echo-Particle Image Velocimetry against 4D Flow MRI in Patients,” *medRxiv*, p. 2023.11.27.23298719, Nov. 2023, doi: 10.1101/2023.11.27.23298719.

[40] F. Maes, A. Collignon, D. Vandermeulen, G. Marchal, and P. Suetens, “Multimodality image registration by maximization of mutual information,” *IEEE Trans Med Imaging*, vol. 16, no. 2, pp. 187–198, 1997, doi: 10.1109/42.563664.